Scaling Potential Evapotranspiration with Greenhouse Warming

JACOB SCHEFF AND DARGAN M. W. FRIERSON

Department of Atmospheric Sciences, University of Washington, Seattle, Washington

(Manuscript received 17 April 2013, in final form 23 September 2013)

ABSTRACT

Potential evapotranspiration (PET) is a supply-independent measure of the evaporative demand of a terrestrial climate—of basic importance in climatology, hydrology, and agriculture. Future increases in PET from greenhouse warming are often cited as key drivers of global trends toward drought and aridity. The present work computes recent and ''business as usual'' future Penman–Monteith PET fields at 3-hourly resolution in 13 modern global climate models. The percentage change in local annual-mean PET over the upcoming century is almost always positive, modally low double-digit in magnitude, usually increasing with latitude, yet quite divergent between models.

These patterns are understood as follows. In every model, the global field of PET percentage change is found to be dominated by the direct, positive effects of constant-relative-humidity warming (via increasing vapor deficit and increasing Clausius–Clapeyron slope). This direct-warming term accurately scales as the PET-weighted (warm-season daytime) local warming, times 5%–6% $°C^{-1}$ (related to the Clausius–Clapeyron equation), times an analytic factor ranging from about 0.25 in warm climates to 0.75 in cold climates, plus a small correction. With warming of several degrees, this product is of low double-digit magnitude, and the strong temperature dependence gives the latitude dependence. Similarly, the intermodel spread in the amount of warming gives most of the spread in this term. Additional spread in the total change comes from strong disagreement on radiation, relative humidity, and wind speed changes, which make smaller yet substantial contributions to the full PET percentage change fields.

1. Introduction

a. Why potential evapotranspiration?

Potential evapotranspiration (PET), a basic land climate variable (e.g., Hartmann 1994), is the rate at which a given climate is trying to evaporate water from the soil–vegetation system. In other words, for given atmospheric and radiative conditions, PET is the surface evapotranspiration (ET) rate that would hold if the soil and vegetation were well watered. Synonymous and near-synonymous concepts include reference evapotranspiration, potential evaporation, evaporative demand, and pan evaporation. Critically, PET may be thought of as the water required to maintain a garden or irrigated crop, or the water ''price'' a plant must pay to maintain open stomata. A higher-PET climate is thus a more arid, evaporative climate. Therefore, in this study we attempt to understand how local PET will scale with global greenhouse warming, using global climate models (GCMs) as well as basic physical principles.

PET is also of interest because it is a key factor explaining other hydrologic and climatic quantities. Several prominent conceptual models of land hydrology, including the Palmer Drought Severity Index (PDSI) (Palmer 1965) and the Budyko and Miller (1974) ecohydrologic theory, take precipitation (water supply) and PET (water demand) as climate-supplied forcings and give soil moisture, actual ET (latent heat) flux, runoff, and/or drought index as land-generated responses. In these sorts of frameworks, understanding precipitation and PET changes is necessary for understanding other land hydroclimatic changes. In particular, recent studies using the PDSI to warn of widespread drought increases with future greenhouse warming (e.g., Dai 2013; Burke et al. 2006) cite systematic global PET increases as the main driver of their alarming results. Understanding the nature, magnitude, and pattern of these projected increases is the motive of the present work.

Additionally, PET is a more natural choice than actual ET for the evaporative component of land ''aridity'' metrics because changes in actual ET often just reflect

Corresponding author address: Jacob Scheff, University of Washington, Department of Atmospheric Sciences, Box 351640, Seattle, WA 98195-1640.
E-mail: jscheff@uw.edu

DOI: 10.1175/JCLI-D-13-00233.1

supply (precipitation) changes. For example, the well-known study of Seager et al. (2007) uses precipitation minus actual ET ($P - E$) to quantify modeled aridification due to greenhouse warming in a subtropical terrestrial region where the model precipitation declines a great deal. The model ET (the Seager et al. E) in this area also significantly declines, not surprisingly. However, the analysis, by its nature, interprets the ET decline as if it is some other factor helping to offset or mitigate the precipitation decline. In fact, the model climate is probably becoming more evaporative, not less, owing to warming and (presumably) cloud-cover and relative-humidity reduction, and this should not mitigate but aggravate the local ecological effect of the precipitation reduction, even though the actual evaporative flux necessarily decreases owing to the supply decrease (e.g., Brutsaert and Parlange 1998). To avoid this type of pitfall, the aridity of a climate is usually quantified using the ratio P/PET of annual water supply to annual water demand, or similar (e.g., Budyko and Miller 1974; Middleton and Thomas 1997; Mortimore 2009), which has the additional advantage of being dimensionless. Then P/PET < 0.05 is defined as hyperarid, $0.05 < P$/PET < 0.2 as arid, $0.2 < P$/PET < 0.5 as semiarid, and so forth. Feng and Fu (2013) show that global climate models project systematic future decreases in P/PET (i.e., aridification) over most of the earth's land, again owing to the (projected) systematic PET increases that we attempt to understand in this work.

b. Quantifying PET

Except where an evaporation pan, lysimeter, or other direct method is available, PET cannot be measured in the field, so it is usually estimated from its meteorological and/or radiative causes. Several estimation methods are in wide use. All of the above studies of greenhouse-driven future drought or aridity expansion (Dai 2013; Burke et al. 2006; Feng and Fu 2013) use the Penman–Monteith equation, a fundamental physics-based method (Penman 1948; Monteith 1981). Given some near-surface air temperature T_a, water vapor pressure e_a, wind speed $|u|$, and net downward broadband radiation R_n, this equation simply gives the latent heat flux (LH) (equivalent to ET) that solves the system:

$$\mathrm{SH} = \frac{\rho_a c_p (T_s - T_a)}{r_a}, \tag{1}$$

$$\mathrm{LH} = \frac{\rho_a c_p [e^*(T_s) - e_a]}{\gamma (r_s + r_a)}, \tag{2}$$

$$R_n - G = \mathrm{SH} + \mathrm{LH} \tag{3}$$

for the three unknowns SH (sensible heat flux), LH, and T_s (skin temperature that would hold under well-watered conditions). Here, (1) is the bulk formula for SH, (2) is the bulk formula for LH under well-watered conditions, (3) is the surface energy budget, $e^*(T)$ is the saturation vapor pressure at a given temperature T, $r_a = 1/(C_H|u|)$ is the aerodynamic resistance between the canopy surface and the level where T_a and e_a are measured, C_H is a scalar transfer coefficient, r_s is the bulk stomatal resistance under well-watered conditions, G is the heat flux into the ground or soil (usually parameterized or ignored), ρ_a is the air density, c_p is the air specific heat, $\gamma = (c_p p_s)/(\varepsilon L_v)$ is the collection of constants from having written (2) in a manner analogous to (1), p_s is the surface air pressure, $\varepsilon \approx 0.622$ is the ratio of molar masses of water vapor and dry air, and L_v is the latent heat of vaporization of water.

The solution to this system proceeds by noting that, if $T_s - T_a$ is not too large, then $e^*(T_s) \approx e^*(T_a) + de^*/dT(T_a)(T_s - T_a)$, which allows T_s to be cleanly eliminated between (1) and (2), giving [with the help of (3)]

$$\mathrm{LH} = \frac{\Delta(R_n - G) + \rho_a c_p [e^*(T_a) - e_a] C_H |u|}{\Delta + \gamma(1 + r_s C_H |u|)}, \tag{4}$$

which is the surface latent heat flux that would hold under well-watered conditions with the given meteorology and radiation. Here $\Delta := de^*/dT(T_a)$ is the standard shorthand for the local slope of the Clausius–Clapeyron curve, which will be used from now on. By definition, this flux (divided by L_v) is the potential evapotranspiration. The resulting Eq. (5) is the *Penman–Monteith equation*:

$$\mathrm{PET} = \left[\frac{\Delta(R_n - G) + \rho_a c_p e^*(T_a)(1 - \mathrm{RH}) C_H |u|}{\Delta + \gamma(1 + r_s C_H |u|)} \right] \Big/ L_v. \tag{5}$$

The first term in the numerator of (5) is known as the *radiative term*, and the second is called the *aerodynamic term*. Note that in the latter we have rewritten $[e^*(T_a) - e_a]$ the *vapor pressure deficit* appearing in (4), as $e^*(T_a)(1 - \mathrm{RH})$, where RH is the near-surface relative humidity. This allows changes in the vapor pressure deficit to be separated into constant-RH changes in e^* (from T_a changes), and constant-T_a changes in RH. [Henceforth we are dropping the (T_a) and simply writing e^* for $e^*(T_a)$, since T_s has been eliminated.]

Many of the input variables in (5) will change with significant greenhouse warming. Most immediately, the surface net radiation R_n will tend to increase (absent any cloud feedbacks) because of the extra longwave emitters

in the atmosphere, sending more longwave energy back at the surface. This alone would tend to increase PET (5). However, the warming itself will also directly change PET through e^* and Δ, which both increase with T_a by the Clausius–Clapeyron law. Constant-RH increases in e^* will increase PET by widening the vapor pressure deficit, especially where and when RH is low. [The discussion in the review paper of Roderick et al. (2009) omitted this mechanism.] Increases in Δ may increase or decrease PET depending on the magnitudes of various terms in (5). It is not clear a priori whether the radiation changes or these direct-warming changes will dominate.

In addition, RH might change in either direction, through a common theoretical expectation for RH is that it should remain roughly constant (e.g., Held and Soden 2000), as generally observed thus far (e.g., Held and Soden 2006). This is the main motivation for considering constant-RH e^* changes separately from changes in RH.

Finally, raw observations indicate that $|u|$ decreased in most land areas over the past several decades (McVicar et al. 2012), in sufficient magnitude to overcome the concurrent T_a increases in (5) and explain the widespread observations of declining pan evaporation, that is, *declining* PET (McVicar et al. 2012; Roderick et al. 2009; Wang et al. 2012). However, it is still unclear whether this terrestrial wind ''stilling'' is a measurement artifact, as it does not appear in reanalyses (e.g., Pryor et al. 2009; McVicar et al. 2008) or marine observations (McVicar et al. 2012), and some of the pan-evaporation declines themselves are also raw and unadjusted for observing-system changes. Even if real, it is highly unclear whether the stilling is due to global warming (McVicar et al. 2012), and it may have reversed course after about 1998 (Wang et al. 2012). Therefore, in this study we take the future model output of $|u|$ at face value, which contains no such systematic declines. However, if any real global stilling trend of the proposed magnitude were to continue unabated into future decades, PET would presumably continue declining and the conclusions of our study (as well as those mentioned above) would not apply.

Other, non-Penman methods of estimating PET are also in use, as mentioned at the beginning of this subsection. The Thornthwaite (1948) method and other *temperature-proxy methods* empirically relate PET to T_a alone, for a given location and time of year. This simplicity has encouraged their frequent use for variability in the current climate (e.g., Palmer 1965), which has led some studies to use them, or models containing them, to assess future climate change (e.g., Wehner et al. 2011; Price and Rind 1994); see also references in Lofgren et al. (2011). However, within a given climate (especially during warm, high-PET parts of the year), anomalous warmth is associated with anomalous sunshine (higher R_n), and often also with anomalous low RH, significantly enlarging the positive response of (5). By contrast, future climate change should warm T_a without the sunshine and RH changes that might accompany a similar warm anomaly in year-to-year variability. Thus one would expect from (5) that an empirically determined dependence of PET on T_a from year-to-year variation would overestimate the greenhouse climate change response. Indeed, several studies (e.g., McKenney and Rosenberg 1993; Hobbins et al. 2008) have found that the same long-term climatic changes can imply large increases in the Thornthwaite PET but much smaller increases, or even slight decreases in Penman–Monteith PET. Similarly, negative PDSI responses to future global climate model output are 2–3 times stronger using the default Thornthwaite PET than using Penman–Monteith PET (A. Dai 2012, personal communication) Thus, studies that use a simple temperature-proxy method to assess future PET changes may be severely flawed.

Other studies of future climate change (Lofgren et al. 2011; Arora 2002) simply estimate PET as R_n/L_v, which we will call the *energy-only method*. While this works reasonably well for spatial differences in the present climate (Budyko and Miller 1974), one would presume that it *underestimates* future PET increases because it does not include the independent physical effects of T_a through the Clausius–Clapeyron law, discussed above.

Still other studies of PET change in global climate models (e.g., Rind et al. 1990) have directly used an internal land-model field that is also called ''potential evapotranspiration.'' However, this field is (quite confusingly) not the same concept as what we have been discussing: it is what would *instantaneously* start evaporating if the surface were to be suddenly wettened, without any chance to cool down the skin temperature T_s and establish energy balance (3) with R_n. In other words, this field is directly computed using the bulk LH Eq. (2), where r_s is still the well-watered ''open'' stomatal resistance but T_s is now the actual skin-temperature output of the model instead of the well-watered skin temperature used above, which is often much cooler. Indeed, Rind et al. (1990) (and references therein) found that this model ''PET'' achieved summertime climatological values averaged over the United States of $\sim$40 mm day^{-1} in the climate models of their day. [The observed summertime PET maxima in, e.g., Hartmann (1994) are almost an order of magnitude lower.] So this quantity, while interesting perhaps, is not the object of our study (and also it is not publicly archived by any of the GCMs in the current phase of the Coupled Model Intercomparison Project).

TABLE 1. CMIP5 models analyzed in this study.

Model acronym	ID on figures	Model and institution
ACCESS1.0[a]	access	Australian Community Climate and Earth-System Simulator, version 1.0; Commonwealth Scientific and Industrial Research Organization (CSIRO) and Bureau of Meteorology (BOM), Australia
BCC-CSM1.1	bcc	Beijing Climate Center (BCC), Climate System Model, version 1.1; Meteorological Administration, China
BCC-CSM1.1-M	bccm	Beijing Climate Center (BCC), Climate System Model, version 1.1, mid resolution
BNU-ESM	bnu	Beijing Normal University (BNU)—Earth System Model; College of Global Change and Earth System Science, Beijing
CNRM-CM5	cnrm	Centre National de Recherches Météorologiques (CNRM) Coupled Global Climate Model, version 5; Centre Européen de Recherche et Formation Avancées en Calcul Scientifique, France
GFDL CM3	gfdl3	Geophysical Fluid Dynamics Laboratory (GFDL) Climate Model, version 3; NOAA, United States
GFDL-ESM2G	gfdleg	GFDL Earth System Model with Generalized Ocean Layer Dynamics (GOLD) component (ESM2G)
GFDL-ESM2M	gfdlem	GFDL Earth System Model with Modular Ocean Model 4 (MOM4) component (ESM2M)
HadGEM2-ES[a,b,c]	had	Hadley Centre Global Environment Model, version 2—Earth System; Met Office, United Kingdom
INM-CM4	inm	Institute of Numerical Mathematics (INM) Coupled Model, version 4.0; Russia
IPSL-CM5A-LR	ipsll	L'Institut Pierre-Simon Laplace (IPSL) Coupled Model, version 5, coupled with NEMO, low resolution; France
IPSL-CM5A-MR	ipslm	IPSL Coupled Model, version 5, coupled with NEMO, mid resolution
MRI-CGCM3	mri	Meteorological Research Institute (MRI) Coupled Atmosphere–Ocean General Circulation Model, version 3; Japan

[a] Surface winds were given on a grid staggered from that of the other surface variables; see section a of the appendix.
[b] Run 2 was used for historical (and run 1 was used for RCP8.5), as these were the only respective runs with 3-hourly output.
[c] 3-hourly surface pressure was not available, so monthly surface pressure output was used for each 3-h interval.

Therefore, in this study we use (5) to quantify and understand the PET response to future greenhouse warming.

2. Methods

The Penman–Monteith potential evapotranspiration (5) is usually many times larger in magnitude during the day than at night because of both R_n and the vapor pressure deficit. Thus, daytime climate changes may affect time-integrated PET much more than nighttime climate changes, so it is desirable to examine diurnally resolved climate and PET. In the recent fifth phase of the Coupled Model Intercomparison Project (CMIP5) (Taylor et al. 2012), subdaily surface output is conveniently accessible for the first time, at 3-hourly resolution. Sixteen of the CMIP5 global climate models archive all of the necessary information (surface energy budget terms and near-surface temperature, moisture, and wind) at this resolution for years 2081–99 in the business-as-usual representative concentration pathway 8.5 (RCP8.5) scenario and 1981–99 in the historical scenario. However, in three of these, the meteorological fields are given at, say, 10 m above the soil surface, instead of 10 m above the canopy top (M. Watanabe 2013, personal communication), making them inapplicable to (1) and (2) [and thus (5)] in forest areas. So, we use the remaining 13 models, which we list in Table 1 along with any model-specific exceptions to our procedures. We use output from run 1 ("r1i1p1" in CMIP5 filenames) only.

A prominent version of (5) is the recent American Society of Civil Engineers (ASCE) standardized reference evapotranspiration equation (Allen et al. 2005), which was explicitly developed for the purpose of standardizing the computation of reference or potential ET for all users. The development included the systematic intercomparison and testing of numerous operationally used Penman-type methods. Our full method closely based on Allen et al. is given in section a of the appendix. Briefly, we fix C_H and r_s as universal constants corresponding to "alfalfa" values as specified by Allen et al. (2005), with $C_H \approx 5.7 \times 10^{-3}$, and r_s varying between $30\,\mathrm{s\,m^{-1}}$ (day) and $200\,\mathrm{s\,m^{-1}}$ (night). (We will see in section 5 that our conclusions are not very sensitive to these vegetation parameters.) We also compute $(R_n - G)$ as LH + SH (3) because the models do not output G, and we let e^*, Δ, and ρ_a depend on T_a as specified in Allen et al.

Using these procedures and values, for each of the 13 CMIP5 models in Table 1 we compute Penman–Monteith

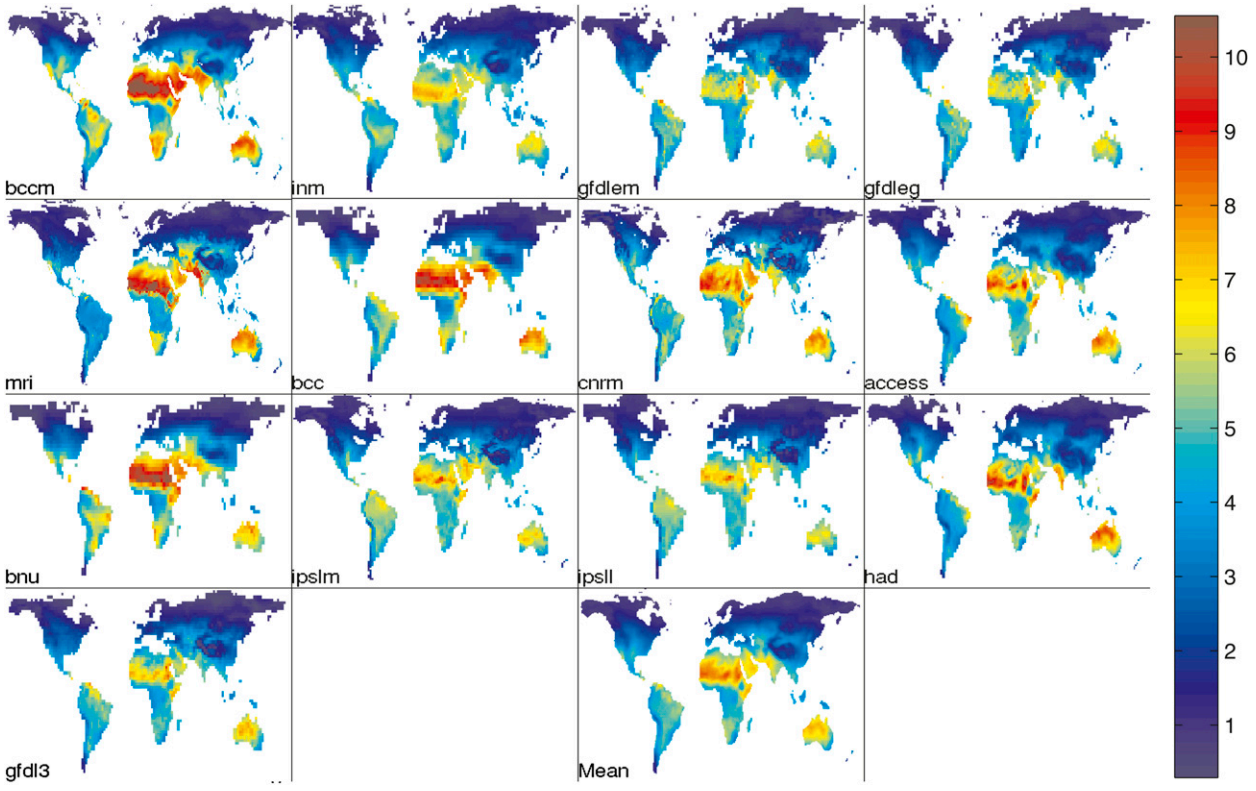

FIG. 1. 1981–99 climatological annual-mean Penman–Monteith PET (mm day^{-1}) for each CMIP5 model in Table 1. Last panel is the mean over all applicable models (omitting locations where less than half of the models were analyzed).

PET (5) for every model grid cell that is at least 80% ice-free land and for every 3-h interval in the 19-yr epochs 1981–99 and 2081–99 (except those that fall on 29 February in models that use the full Gregorian calendar). For each interval in the calendar year, we average over the 19 years to obtain a diurnally and annually varying PET climatology of each epoch. Averaging over the calendar then gives annual-mean climatologies of PET. These are shown for 1981–99 in Fig. 1 along with their multimodel means and appear quite reasonable with higher modeled PET in sunnier, lower-RH, and/or warmer locations. As an additional reality check, Fig. 2 plots these against the corresponding model climatologies of actual ET; each dot is one grid cell. In almost all of the models, our computed PET is a fairly clean, efficient upper bound on the model's actual ET, as expected from the definition. That is, the most well-watered model grid cells are actually evapotranspiring at rates quite close to our independently computed PET. This success is a rather pleasant surprise considering the very different origins of the two quantities, the models' use of full Monin–Obukhov surface layer dynamics for C_H, and the potentially large contrast between ASCE-standard alfalfa and the vegetation specified in the model grid cells.

3. Model results

a. Full PET change

For each of the 13 models and for the multimodel mean, Fig. 3 maps the raw percentage change in climatological annual-mean PET (5) between the 1981–99 and 2081–99 epochs. At each location PET always or almost always increases; that is, ambient conditions become more evaporative with greenhouse warming. This more careful calculation confirms the similar results of Burke et al. (2006), Dai (2013), and Feng and Fu (2013), who quantified this future PET increase only for the mean (or for a single model), and did not resolve the diurnal cycle. In some models a few largely high-latitude regions do see PET decreases or little change in PET, but these are quite localized, and even in these places most models (and the mean) show increases in PET.

Furthermore, the magnitude of the projected PET increases is usually in the low double digits of percent, on the order of 10%–45%. In many models certain northern and/or mountainous locations see more than this, but over very broad swaths of land these sorts of values are typical. For the multimodel mean, the first row of Table 2 summarizes this by averaging the percentage change values over various latitude bands (and

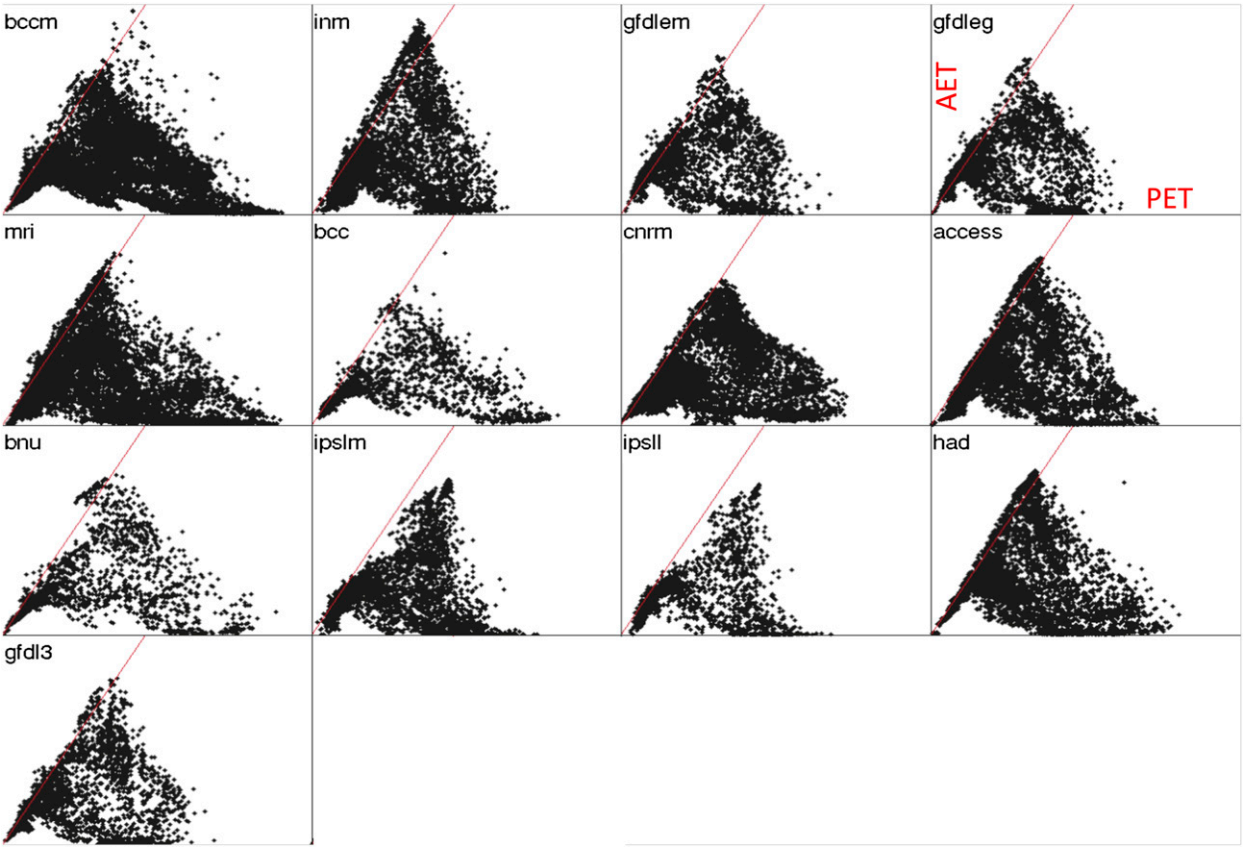

FIG. 2. 1981–99 climatological annual-mean actual ET (vertical, 0–6 mm day^{-1}) vs PET (horizontal, 0–13 mm day^{-1}) for each model, where each dot is one grid cell. Red lines are 1:1 (actual ET = PET).

subsequent rows similarly average subsequent figures). The magnitudes in Fig. 3 agree well with those in Feng and Fu (2013) despite the differing methods. They are also comparable to change magnitudes for annual precipitation P (e.g., Meehl et al. 2007). This further confirms the importance of using P/PET or similar diagnostics when thinking about the land aridity response to global warming, instead of just P (and/or actual evapotranspiration E, which often contains the same information as P as discussed in section 1a).

In most models and in the mean, there is also a clear tendency toward greater percentage increases in PET at higher latitudes (as alluded to above and seen in Table 2), and again Feng and Fu (2013) obtain a similar structure. As far as we know, this basic property has not been explicitly noted in the literature before. (We will see in section 4 that the main reason for this is not Arctic amplification of warming.)

Yet despite all of these broad commonalities, the models also disagree a great deal, on both the detailed spatial patterns and the overall magnitude. We will see how these disagreements arise from differences in the climate changes projected by the models.

b. PET changes due to individual factors

Figures 4, 5, 6, and 7 show the percent changes in climatological annual-mean PET (5) that result from perturbing ($R_n - G$), T_a, RH, and $|u|$ one at a time to 2081–99 levels while keeping the other variables at 1981–99 levels, as explained in detail in section b of the appendix. One can immediately see here and in Table 2 that the always-positive PET change owing to the T_a increase (Fig. 5) dominates the other factors in most locations, and explains most of the overall 10%–45% magnitude in Fig. 3. This is why PET increases are so much more common than decreases. Again, the physical mechanisms here are widening of the vapor pressure deficit by constant-RH increases in e^*, and lowering of the saturated Bowen ratio by increases in Δ (plus isobaric lowering of ρ_a to a small extent). RH also changes, but the resulting PET changes (Fig. 6) are of both signs, inconsistent from model to model, very weakly positive in the multimodel mean, and only sporadically (nowhere, in the mean) negative enough to cancel the T_a-induced increases in Fig. 5. This validates the constant-RH baseline idea and justifies our decision

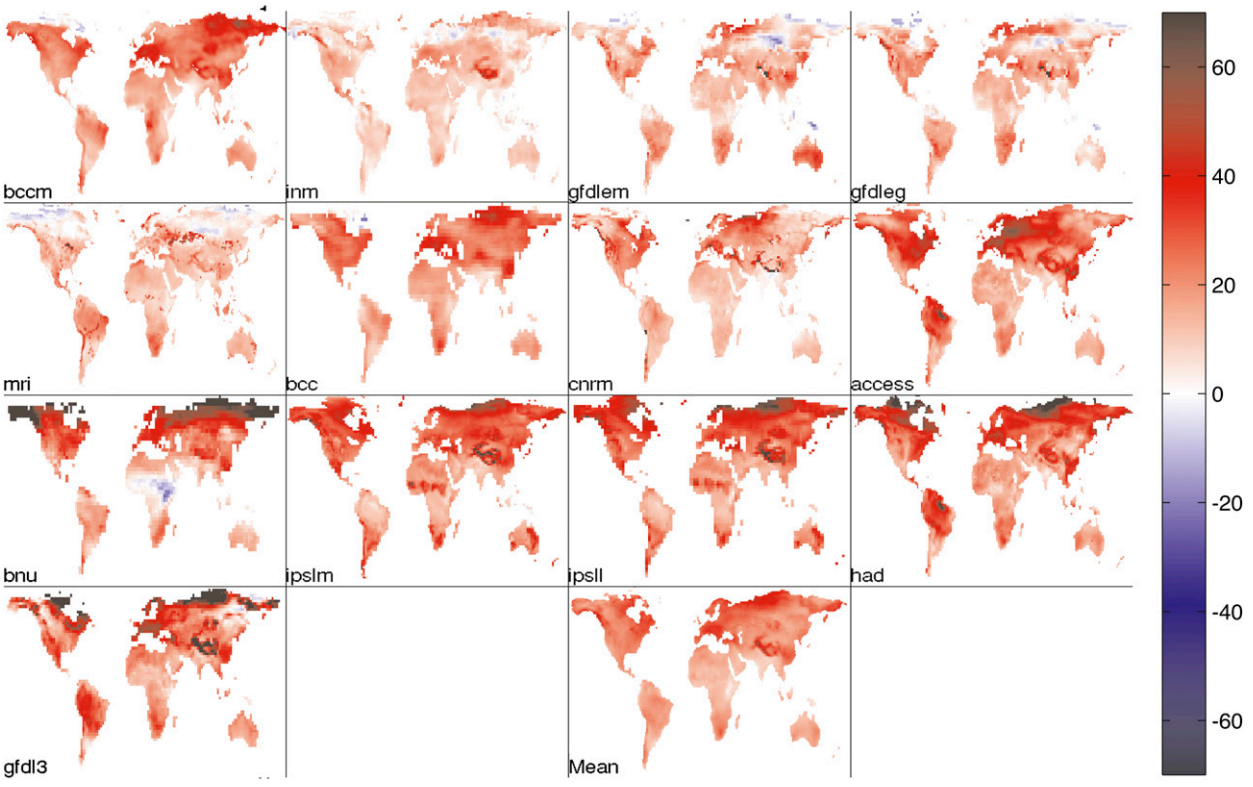

FIG. 3. Percent changes in climatological annual-mean PET between 1981–99 and 2081–99, for each model. (Values in a few color-saturated regions greatly exceed those on the scale.) Last panel is the percentage change in the multimodel mean.

to think of the vapor pressure deficit as $e^*(1 - \mathrm{RH})$ rather than the more customary $(e^* - e_a)$. (An alternative null assumption of constant vapor pressure deficit would imply systematically increasing RH, which we do not see.) However, the RH-driven changes can still be very important locally in some models, explaining the East African PET decrease in BNU-ESM in Fig. 3, for example.

PET changes owing to the surface energy supply $(R_n - G)$ (Fig. 4) are also usually positive, confirming the physical intuition from section 1b. However, with modal values of less than 10% (e.g., Table 2) they are generally of secondary importance to the Clausius–Clapeyron-driven changes (Fig. 5) just described. This was not clear a priori—in fact, some studies in the literature had used radiation changes alone to infer PET changes, as discussed above in section 1b. As with RH, though, some models have localized regions where radiation-induced change becomes dominant, such as the Amazon Basin in MRI-CGCM3 (and several other models) or the Tibetan Plateau in INM-CM4 (cf. Figs. 3–5).

In contrast, PET responses to $|u|$ changes (Fig. 7) are only rarely important compared to the other changes. In

TABLE 2. Results for the multimodel mean, averaged over different latitude bands.

Fig.	Quantity	60°–15°S	15°S–15°N	15°–40°N	40°–80°N
3	% change in PET	16.9	14.0	17.8	24.4
4	% change in PET due to $(R_n - G)$	1.7	3.0	2.6	5.1
5	% change in PET due to T_a	9.7	7.1	12.5	17.6
13	% change in PET due to T_a (scaling)	10.6	7.7	13.5	19.1
6	% change in PET due to RH	3.4	1.9	1.8	2.5
7	% change in PET due to $\lvert u\rvert$	1.0	0.7	0.1	−0.7
8	% change in PET (residual)	1.0	1.3	0.8	−0.2
14	% change in PET due to T_a if $r_s \equiv 0$	7.0	5.4	9.0	15.2
10	PET-weighted-mean T_a (°C)	24	27	23	13
9	PET-weighted-mean f_Δ (see section 4)	0.61	0.69	0.59	0.48
11	Analytic PET sensitivity to T_a (% °C^{-1})	2.2	1.7	2.4	3.2
12	PET-weighted-mean warming (°C)	4.5	4.4	5.2	5.5

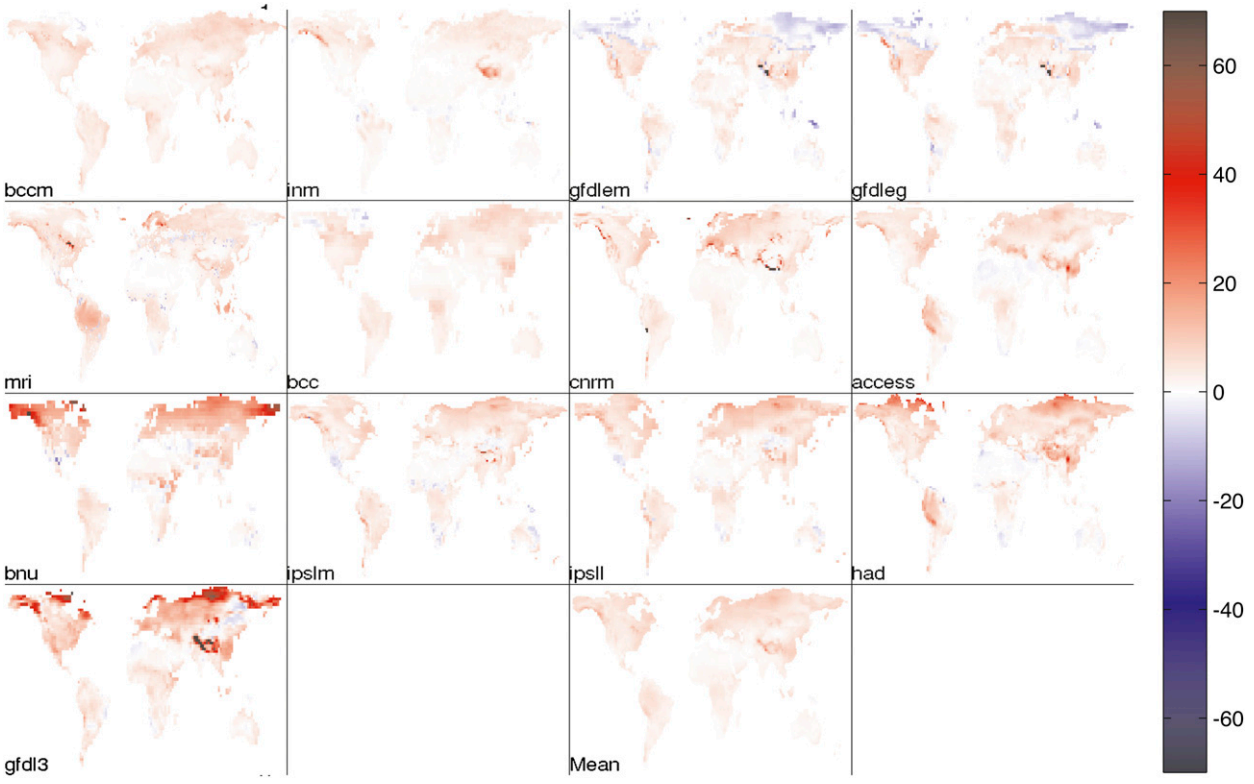

FIG. 4. Percent changes in climatological annual-mean PET from setting only the surface radiative energy supply ($R_n - G$) to 2081–99 levels while leaving all other variables in (5) at 1981–99 levels.

the multimodel mean and in some individual models (the two BCC models, CNRM-CM5, and INM-CM4), they are hardly noticeable, usually no larger than ±5%. Like the RH responses (Fig. 6) they have no strongly preferred sign, although decreases are perhaps slightly more common than increases. This is all in stark contrast to the dominant ''stilling'' role posited for $|u|$ in the putative recent PET declines, discussed in section 1b.

Finally, subtracting the sum of these attributed pieces (Figs. 4–7) from the full PET change (Fig. 3) gives the residual PET change due to nonlinearities, covariance changes, and changes in neglected inputs such as p_s. This residual is shown in Fig. 8 and is quite weak (0%–10%) compared to the T_a-driven or even ($R_n - G$)-driven changes, though it is usually positive. (The GFDL-CM3 residual at high northern latitudes is a major exception to both of these statements, perhaps because the changes there in Figs. 3–6 are all so large.) In any case, we can clearly claim success in our attribution exercise since the residuals are much smaller than the full changes in Fig. 3 and are close to zero for the multimodel mean.

Having now examined all of the pieces, we can see that the constant-RH PET response to temperature change (Fig. 5) not only explains the general positivity and low-double-digit magnitude of the full PET change, but is also largely responsible for the high-latitude amplification noted in the previous subsection. The response to ($R_n - G$) (Fig. 4) is also polar amplified, but the temperature response still seems to contain most of the latitudinal contrast shown in Fig. 3, as can be clearly seen in Table 2. As for the intermodel disagreement in PET change, responsibility seems to lie with almost all of the terms, but disagreement in the T_a-driven term alone is still large, especially in the overall magnitude. [This makes sense given the well-known disagreement between global climate models on the magnitude of warming in response to an emissions scenario, that is, transient climate sensitivity (e.g., Meehl et al. 2007).]

Therefore, we now attempt a detailed quantitative understanding of the structure and magnitude of this model PET response to ambient temperature change as depicted in Fig. 5.

4. Analytic scaling for the PET response to temperature

a. Basic idea

How, exactly, is Penman–Monteith PET (5) sensitive to T_a with all else constant? First, one can note that in the numerator of (5) *both* the aerodynamic term and the

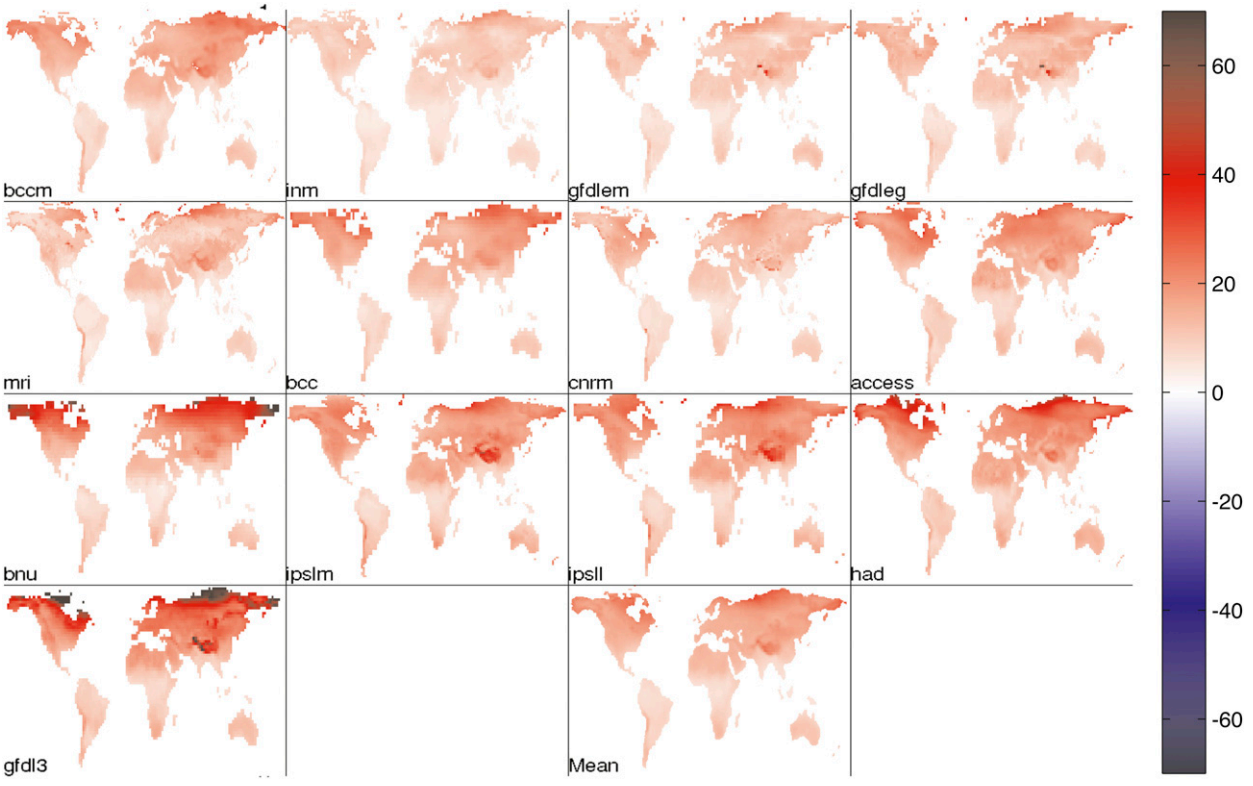

FIG. 5. Percent changes in climatological annual-mean PET from setting only the ambient air temperature T_a (and thus the saturation vapor pressure e^* and its derivative Δ) to 2081–99 levels while leaving all other variables in (5), including RH, at 1981–99 levels.

radiative term increase roughly like Clausius–Clapeyron (C-C) with T_a at constant RH because $e^*(T)$ is a roughly exponential function, so $\Delta := de^*/dT$ has roughly the same fractional rate of increase with T as e^* does. More precisely [and using the empirical form from Allen et al. (2005) and the appendix for consistency]:

$$e^* = 610.8 \exp\left(\frac{17.27T}{T + 237.3}\right), \tag{6}$$

$$\Delta = \frac{de^*}{dT} = \frac{17.27 \times 237.3 e^*}{(T + 237.3)^2}; \tag{7}$$

so

$$\begin{aligned} \frac{d\Delta}{\Delta dT} &= \frac{d \ln \Delta}{dT} \\ &= \frac{d[\ln(17.27 \times 237.3) + \ln e^* - 2\ln(T + 237.3)]}{dT} \\ &= \frac{de^*}{e^* dT} - \frac{2}{T + 237.3}, \end{aligned} \tag{8}$$

where T is in degrees Celsius and e^* in pascals. At earthlike temperatures $de^*/(e^* dT)$ is around 6%–7% °C^{-1} but $2/(T + 237.3)$ is only 0.7%–0.8% °C^{-1}, so (8) means that $d\Delta/(\Delta dT)$ is not far from $de^*/(e^* dT)$ at all. [These values still hold using the physical C-C equation in place of the empirical (7).] So, all else constant, we can expect the entire numerator of PET (5) to increase at a C-C-like rate with warming of T_a, regardless of the relative importance of the radiative and aerodynamic terms. This is why we did not further split the response to T_a into responses to e^* and Δ in section 3b above.

However, the denominator of (5) cannot necessarily increase so fast: although Δ increases at roughly C-C as demonstrated, $\gamma(1 + r_s C_H |u|)$ does not depend on T_a at all. This term stops the denominator from fractionally increasing as fast as the numerator and apparently is the key reason why PET always increases with T_a (Fig. 5) despite the ambiguous sign of the Δ-driven response discussed in section 1b. If not for the presence of $\gamma(1 + r_s C_H |u|)$, the denominator would increase about as fast as the numerator, and PET might not be very sensitive to T_a at all.

b. Derivation and exposition of the scaling

To quantify all of this, we now take the relative partial derivative of (5) with respect to T_a, repeatedly using the rules

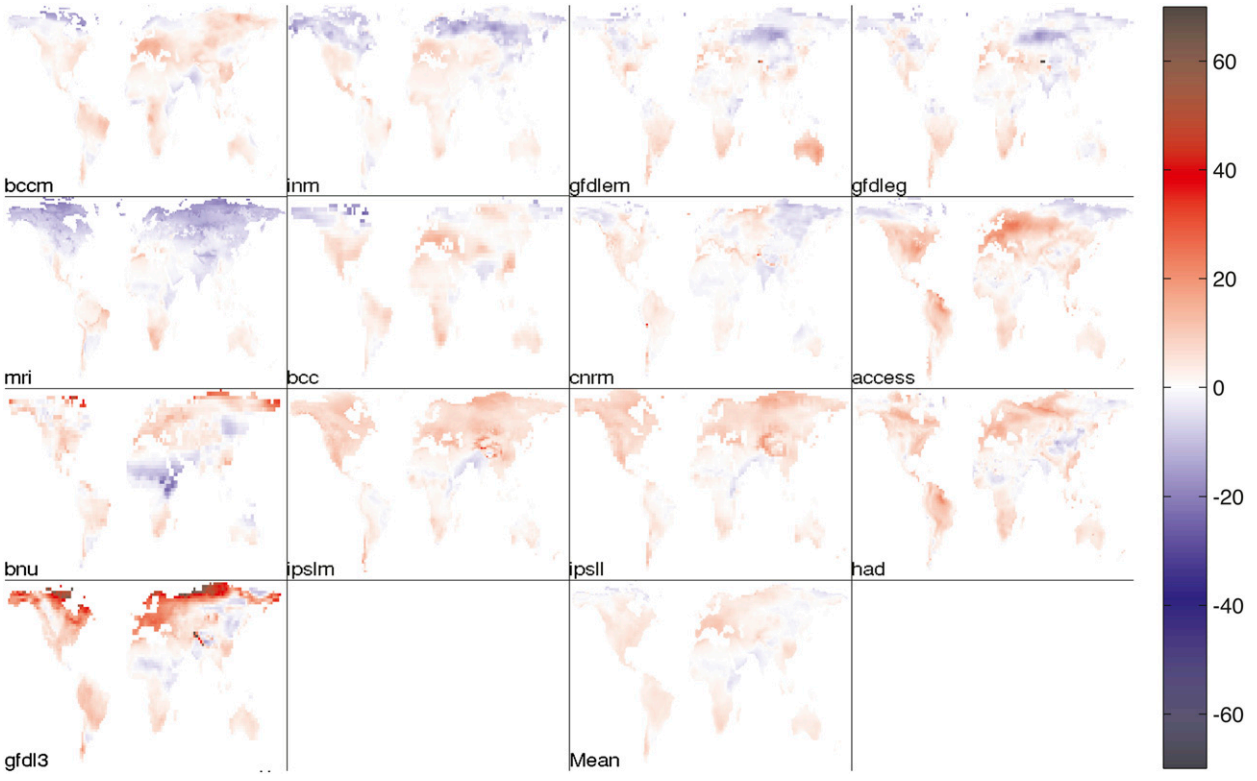

FIG. 6. As in Fig. 4, but setting only the relative humidity to 2081–99 levels.

$$\frac{d(a+b)}{a+b} = \frac{da}{a} f_a + \frac{db}{b} f_b, \tag{9}$$

where $f_a := a/(a + b)$ and $f_b := b/(a + b)$, and

$$\frac{d(a/b)}{a/b} = \frac{da}{a} - \frac{db}{b}, \tag{10}$$

plus the chain rule, to yield

$$\frac{d\mathrm{PET}}{\mathrm{PET}} = dT_a \left[\frac{d\Delta}{\Delta dT} f_{\mathrm{rad}} + \left(\frac{de^*}{e^* dT} + \frac{d\rho_a}{\rho_a dT} \right) f_{\mathrm{aero}} - \frac{d\Delta}{\Delta dT} f_\Delta \right]. \tag{11}$$

Here f_{rad} is the fraction of the numerator of (5) made up by the radiative term, as in (9). Similarly, f_{aero} is the fraction of the numerator made up by the aerodynamic term, and f_Δ is the fraction of the denominator of (5) made up by Δ.

We then use (8) to write $de^*/(e^* dT)$ in terms of $d\Delta/(\Delta dT)$:

$$\frac{d\mathrm{PET}}{\mathrm{PET}} = dT_a \left[\frac{d\Delta}{\Delta dT} f_{\mathrm{rad}} + \left(\frac{d\Delta}{\Delta dT} + \frac{2}{T_a + 237.3} \right) f_{\mathrm{aero}} + \frac{d\rho_a}{\rho_a dT} f_{\mathrm{aero}} - \frac{d\Delta}{\Delta dT} f_\Delta \right]. \tag{12}$$

Using $f_{\mathrm{rad}} + f_{\mathrm{aero}} = 1$ and the ideal-gas-law formula for ρ_a, this reduces to

$$\frac{d\mathrm{PET}}{\mathrm{PET}} = dT_a \left[\frac{d\Delta}{\Delta dT} (1 - f_\Delta) + \left(\frac{2}{T_a + 237.3} - \frac{1}{T_a + 273.15} \right) f_{\mathrm{aero}} \right], \tag{13}$$

the main equation that we will use to understand the constant-RH PET response to T_a as depicted in Fig. 5.

The first term within the brackets in (13) tells the story laid out in the previous subsection: the numerator of PET (5) scales like C-C $[d\Delta/(\Delta dT) \cdot 1]$ or about 5–6% $^\circ\mathrm{C}^{-1}$, but the denominator $\Delta + \gamma(1 + r_s C_H |u|)$ scales closer and closer to C-C the more important Δ is in it $[-d\Delta/(\Delta dT) \cdot f_\Delta]$, weakening the net response. Since Δ is an increasing function of T_a, this cancellation should occur more (f_Δ should be larger and the denominator should be more C-C-like) in warmer base climates, so the percentage sensitivity of PET to T_a should be less in warmer base climates. We will see in section 4d that this explains the polar-amplified response pattern in Fig. 5. (Similarly, the sensitivity should be greater in windier climates, in which f_Δ is reduced.)

The second term within the brackets in (13) contains the small, miscellaneous departures from the above: the

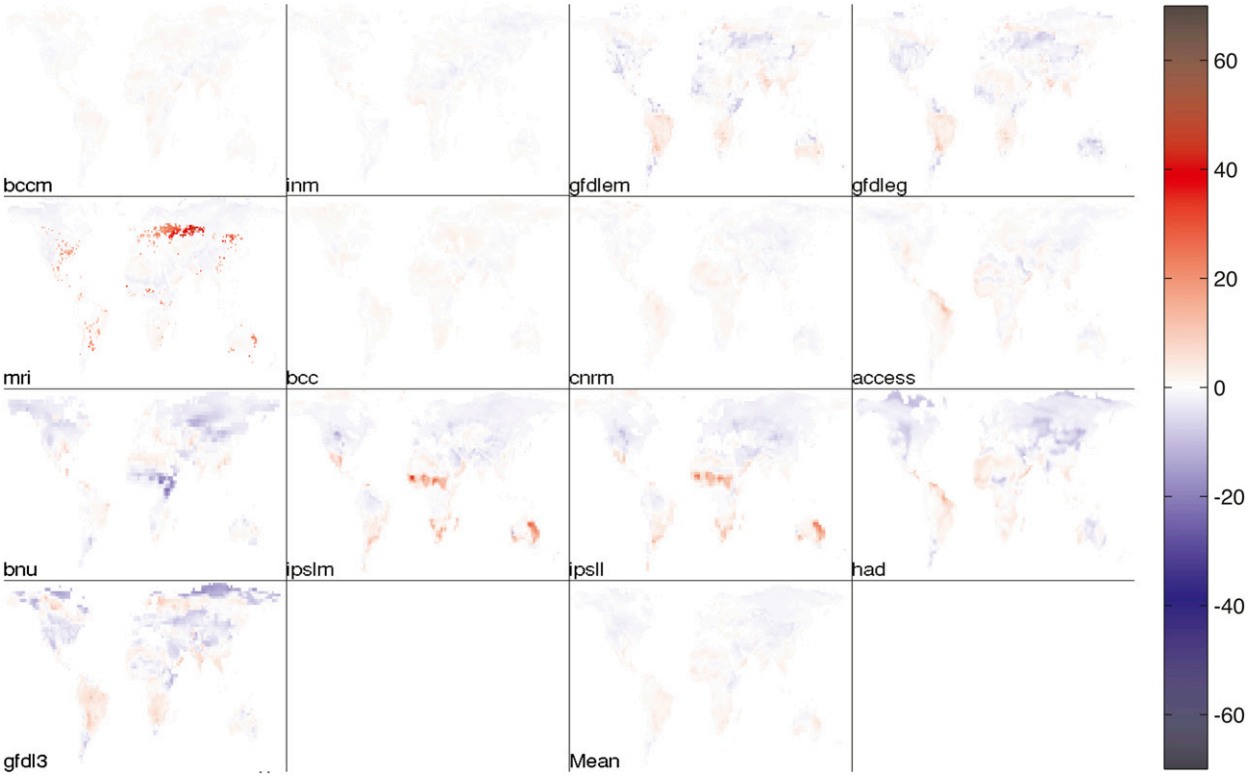

FIG. 7. As in Fig. 4, but setting only the wind speed $|u|$ to 2081–99 levels.

0.7%–0.8% °C^{-1} discrepancy between the scalings of e^* and Δ in the numerator, and the −0.3%–0.4% °C^{-1} isobaric dependence of air density on temperature. The partial cancellation between these two effects makes the net even smaller, ~0.4% °C^{-1} at the most since f_{aero} can only range between 0 and 1. Therefore, from here on we define $\epsilon(T) := 2/(T + 237.3) - 1/(T + 273.15)$ and write

$$\frac{d\text{PET}}{\text{PET}} = dT_a\left[\frac{d\Delta}{\Delta dT}(1 - f_\Delta) + \epsilon(T_a)f_{\text{aero}}\right], \qquad (14)$$

for convenience.

c. *From instantaneous to annual-mean scaling*

Our Eq. (14) may be a theory for PET sensitivity at a particular instant. However, the results from section 3 and Fig. 5 that we wish to understand are about annually averaged PET. So, to test (14) it is not immediately clear what inputs should be used. For example, we might use the annual-mean warming $\overline{dT_a}$. (From here on, an overbar will denote the annual mean.) However, if the warming in some place is, say, 6°C at night but 2°C during the day, then using the mean value of 4°C will overestimate the response because the vast majority of PET is concentrated during the day when the warming is only 2°C. So, we need to carefully consider the scaling of the annual mean, $\overline{\text{PET}}$, in addition to the instantaneous PET considered earlier in this section.

The relative change in $\overline{\text{PET}}$ turns out to be the *PET-weighted average* of the relative change in instantaneous PET. This is because, again, the more PET is concentrated at a particular time, the more a percentage change in PET at that time matters to the percentage change in $\overline{\text{PET}}$. Mathematically,

$$\frac{d\overline{\text{PET}}}{\overline{\text{PET}}} = \frac{\overline{d\text{PET}}}{\overline{\text{PET}}} = \frac{\overline{(d\text{PET}/\text{PET})\text{PET}}}{\overline{\text{PET}}} := \overline{\overline{(d\text{PET}/\text{PET})}}, \qquad (15)$$

where from here on a double overbar denotes a PET-weighted annual average, $\overline{\overline{a}} := \overline{a \cdot \text{PET}}/\overline{\text{PET}}$ for any variable a. So, using (14),

$$\frac{d\overline{\text{PET}}}{\overline{\text{PET}}} = \overline{dT_a\left[\frac{d\Delta}{\Delta dT}(1 - f_\Delta) + \epsilon(T_a)f_{\text{aero}}\right]}. \qquad (16)$$

Essentially, we need to evaluate (14) at times of the day and year when PET is large. This suggests the following simple approximation to (16):

$$\frac{d\overline{\text{PET}}}{\overline{\text{PET}}} \approx \overline{\overline{dT_a}}\left[\frac{d\Delta}{\Delta dT}(\overline{\overline{T_a}})(1 - \overline{\overline{f_\Delta}}) + \epsilon(\overline{\overline{T_a}})\overline{\overline{f_{\text{aero}}}}\right]. \qquad (17)$$

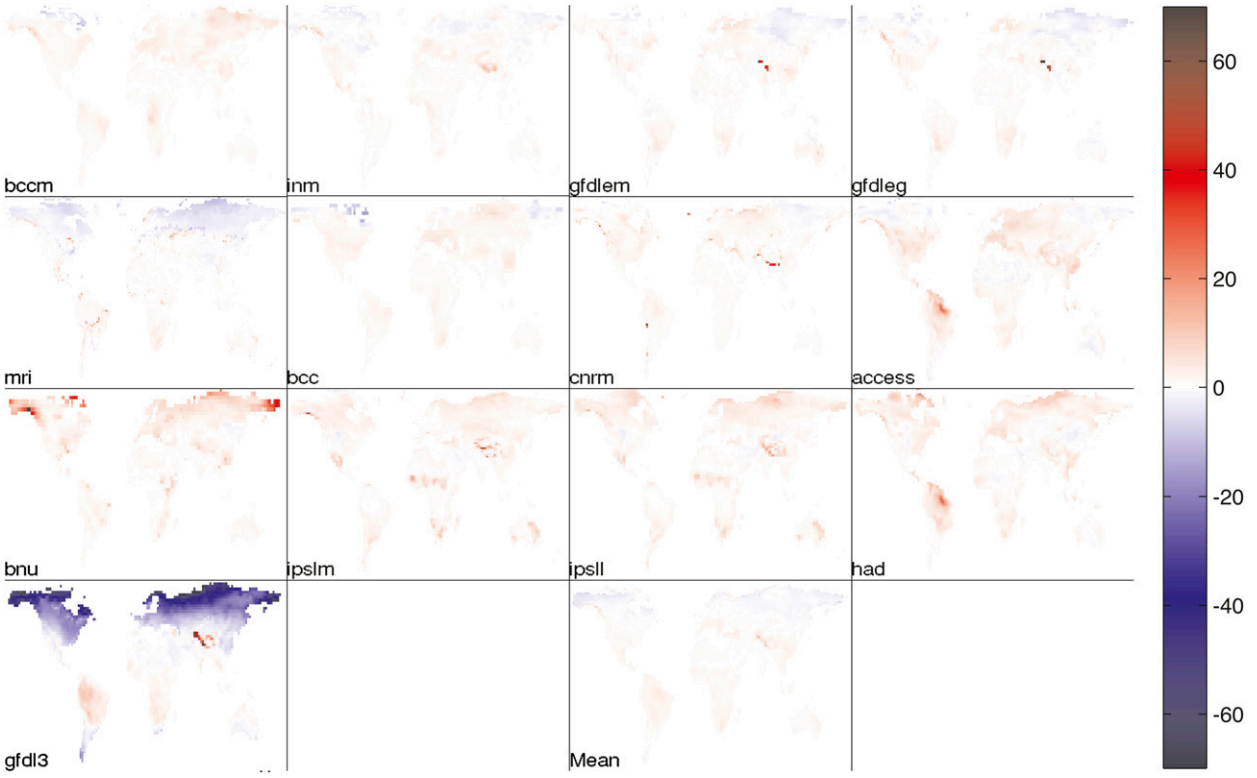

FIG. 8. Residual percentage changes in climatological annual-mean PET between 1981–99 and 2081–99 that remain after subtracting off the pieces attributed to $(R_n - G)$, T_a, RH, and $|u|$ (Figs. 4–7) from the raw change (Fig. 3).

d. Testing the annual-mean scaling

To test this scaling theory (17), we compute $\overline{\overline{dT_a}} = \overline{dT_a \cdot \mathrm{PET}}/\overline{\mathrm{PET}}$, $\overline{\overline{f_\Delta}} = \overline{f_\Delta \cdot \mathrm{PET}}/\overline{\mathrm{PET}}$, and so forth for each model grid cell. For the base-state variables PET, f_Δ, and T_a, we just use diurnally and annually varying 1981–99 climatologies computed as in section 2, not the full 19-yr time series. Similarly, for the change dT_a, we use the same smoothed diurnally and annually varying climatological difference that we used to produce Fig. 5, as detailed in section b of the appendix. (Note that $\overline{\overline{f_{\mathrm{aero}}}}$ turns out to simply be the fraction of annual-total PET that comes from the aerodynamic term, so we compute aerodynamic and radiative $\overline{\mathrm{PET}}$ separately, and directly use this fraction.)

Since $d\Delta/(\Delta dT)$ is not that dependent on temperature and $\epsilon\overline{\overline{f_{\mathrm{aero}}}}$ is small, the main sensitivity "wild card" in (17) should be $\overline{\overline{f_\Delta}}$, the fraction of the denominator of (5) made up by Δ at high-PET times of day and year. The $\overline{\overline{f_\Delta}}$ determines whether the denominator will keep up with the numerator's Clausius–Clapeyron pace and curtail the PET increase with warming, or lag behind it and allow a large PET increase.

So, in Fig. 9 we map $\overline{\overline{f_\Delta}}$ for each model, as well as the multimodel mean of $\overline{\overline{f_\Delta}}$ (summarized in Table 2, as above). One can see that it dramatically varies from as low as ~0.25 in the cool-summer climates of the coastal high latitudes to ~0.75 in the warm climates of the tropics. Apparently the strong dependence of Δ on temperature is in control of this fraction, even though it also depends on quantities in the denominator's other term ($|u|$ and our day length–dependent r_s). Indeed, Fig. 10 shows that the PET-weighted (i.e., daytime, warm-season) basic-state temperature $\overline{\overline{T_a}}$ has a strikingly similar spatial pattern to this $\overline{\overline{f_\Delta}}$, often even at very fine spatial scales. Essentially, in cool, low-Δ climates the denominator of (5) is mainly made up of $\gamma(1 + r_s C_H|u|)$, which stays fixed with T_a and lets (5) increase, while in warm climates it is dominated by Δ, which scales like C-C and cancels most of the numerator's attempt to increase PET.

Figure 11 then maps the entire bracketed term from (17), that is, our scaling estimate of the percentage sensitivity of $\overline{\mathrm{PET}}$ to PET-weighted warming. As guessed, its pattern is nearly the same as that of $\overline{\overline{f_\Delta}}$ (Fig. 9) [and thus $\overline{\overline{T_a}}$ (Fig. 10)], varying from around 1.5% $^\circ\mathrm{C}^{-1}$ over large areas of the planet's warm, high-$\overline{\overline{f_\Delta}}$ tropics to nearly C-C in the coolest-summer regions where $\overline{\overline{f_\Delta}}$ is small and the numerator in (5) can increase nearly unopposed. The models agree on all of these fields much more than they

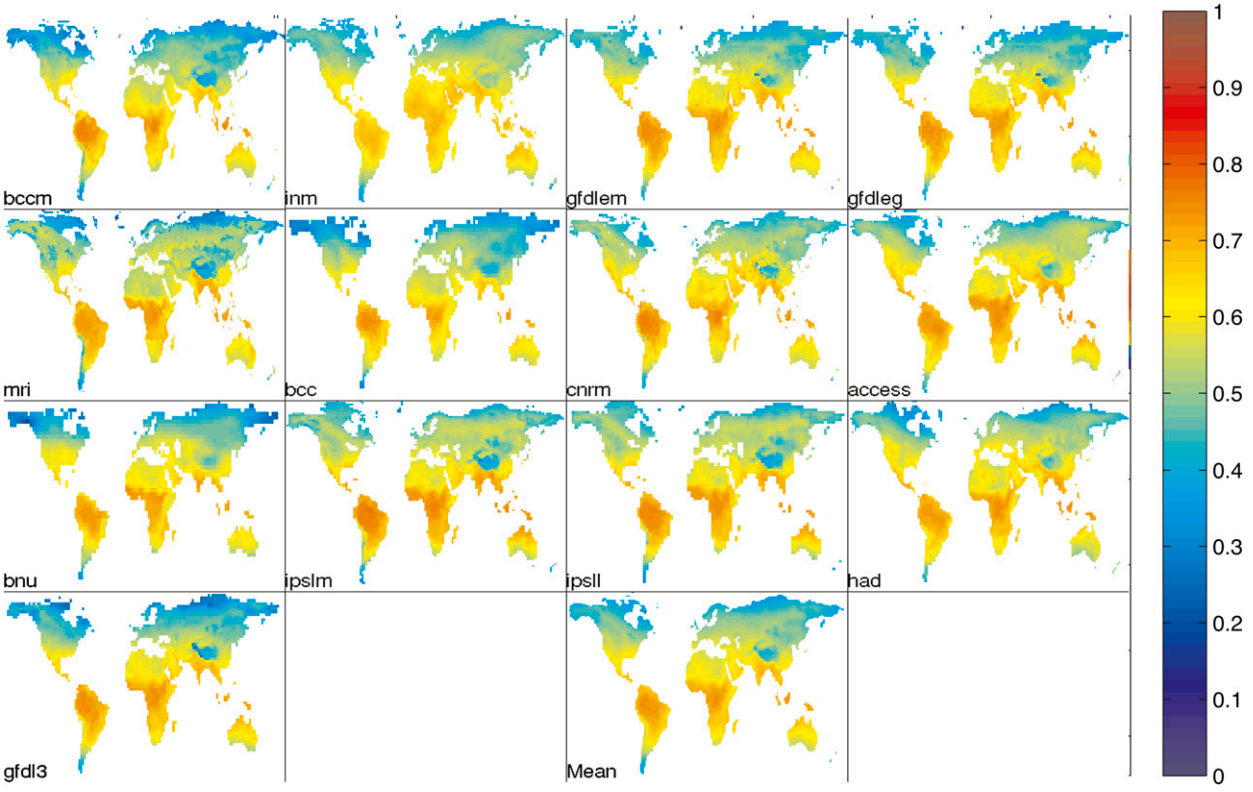

FIG. 9. For each model grid cell, the PET-weighted annual average $\overline{\overline{f_\Delta}}$ of 1981–99 climatological f_Δ, the fraction of the denominator of Penman–Monteith PET (5) made up by the Clausius–Clapeyron slope Δ. The last panel is the multimodel mean.

agree on the gross response to T_a change depicted in Fig. 5. This is not surprising since these are only based on properties of the modeled 1981–99 base climates, which can be tuned to match observations.

On the other hand, the PET-weighted projected warming $\overline{\overline{dT_a}}$ [the other factor in (17)] might vary considerably from model to model since the models do not agree on the warming response to a given greenhouse-gas forcing scenario (e.g., Meehl et al. 2007). Figure 12 maps $\overline{\overline{dT_a}}$ for each model and for the mean, confirming that the spread in modeled warming is much larger than the spread in estimated sensitivity to that warming (Fig. 11). Taking the end members, $\overline{\overline{dT_a}}$ over land seems to be almost three times stronger in GFDL-CM3 than in INM-CM4! Thus it appears that the main reason for the intermodel spread in the magnitude of the $\overline{\text{PET}}$ change due to warming (Fig. 5), noted in section 3b, is indeed the intermodel spread in the warming itself.

We are also now in a position to evaluate the source of the high-latitude amplification of the $\overline{\text{PET}}$ percentage change pattern in Fig. 5, and thus in Fig. 3. Figure 12 shows that the PET-weighted warming $\overline{\overline{dT_a}}$ is, indeed, strongly Arctic amplified in some models (e.g., BNU-ESM and GFDL-CM3). However, in many other models this pattern is absent, even though it is well known that the Arctic amplification of the *annual-mean* warming $\overline{dT_a}$ is robust across climate models (e.g., Meehl et al. 2007). For example, in ACCESS1.0 $\overline{\overline{dT_a}}$ maximizes in midlatitude North America and Europe and in the Amazon Basin, and in GFDL-ESM2G and GFDL-ESM2M $\overline{\overline{dT_a}}$ maximizes in the subtropics. So $\overline{\overline{dT_a}}$ does not consistently show high-latitude amplification, and in the multimodel mean any such amplification is quite weak (Fig. 12; Table 2). This is probably because high-latitude warming amplification is more of a cold-season than a warm-season phenomenon (Meehl et al. 2007), while a PET-weighted mean is largely over the warm season. In contrast, the sensitivity factor in (17), depicted in Fig. 11, shows strong and systematic high-latitude amplification because of the strong control of $\overline{\overline{f_\Delta}}$ (Fig. 9) by the basic-state temperature $\overline{\overline{T_a}}$ (Fig. 10), as discussed above. Thus it appears that $d\overline{\text{PET}}/\overline{\text{PET}}$ (Figs. 5 and 3) is polar amplified not because the warming is polar amplified, but rather largely because colder climates with Δ less important in the denominator of PET are inherently more sensitive (cf. the last two lines of Table 2).

Finally, we can confirm this picture by evaluating (17) and comparing to the model $\overline{\text{PET}}$ responses to T_a

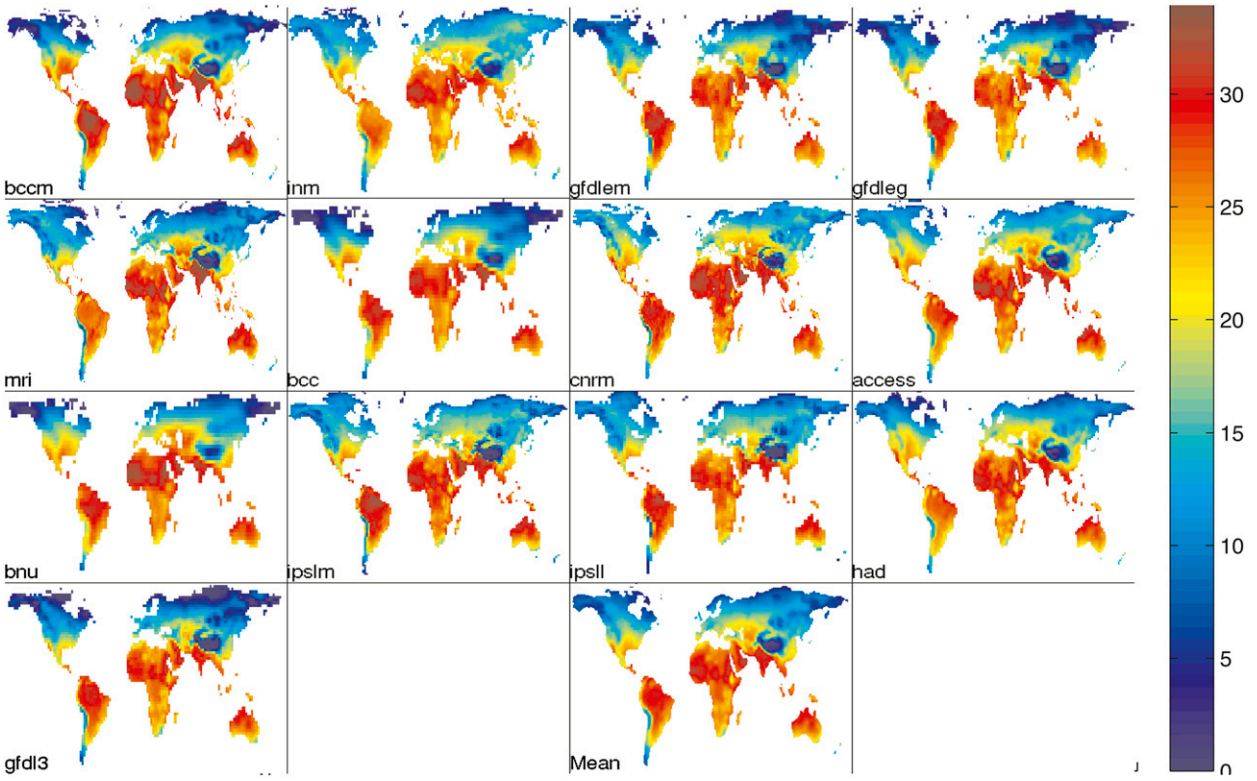

FIG. 10. For each model grid cell, the PET-weighted annual average 1981–99 climatological temperature $\overline{\overline{T_a}}$, in °C. The last panel is the multimodel mean.

changes in Fig. 5. Before displaying the result, we need to note that, if the sensitivity factor in (17) is, e.g., 4% $°C^{-1}$ and the projected warming $\overline{\overline{dT_a}}$ is 9°C, the expected $\overline{\text{PET}}$ change should be noticeably larger than 36% because $1.04^9 \approx \exp(0.36) > 1.36$. To account for this simple nonlinearity, we exponentiate (17) and subtract 1 to arrive at our final scaling guess for what Fig. 5 should look like.

This estimate is shown in Fig. 13 and is strikingly close to the model response in Fig. 5. In fact, the summary values in Table 2 differ from the actual values on the line above by only about +1% (of the basic state, about 10% of the changes). Thus, we can claim success in understanding the magnitude, structure, and intermodel spread in Fig. 5. The low double-digit percent magnitude of $d\overline{\text{PET}}/\overline{\text{PET}}$ comes from the mid-single-digit °C greenhouse warming (Fig. 12) times the sub-Clausius–Clapeyron, 1%–4.5% $°C^{-1}$ sensitivity of (5) at constant RH (Fig. 11 and sections 4a,b). The structure of $d\overline{\text{PET}}/\overline{\text{PET}}$ comes mainly from the structure of the base-climate temperature $\overline{\overline{T_a}}$ (Fig. 10) via $\overline{\overline{f_\Delta}}$ (Fig. 9) and the sensitivity (and also somewhat from the structure of the warming). The intermodel spread comes from the intermodel spread in the warming.

5. Sensitivity of results to imposed vegetation

One might wonder whether the above holds for parameter choices in (5) other than the ones presented in section 2 and the appendix. In particular, the transfer coefficient C_H and bulk stomatal resistance r_s could potentially modulate the T_a-independent term $\gamma(1 + r_s C_H|u|)$ in the denominator of (5), and therefore alter $\overline{\overline{f_\Delta}}$ and the bracketed sensitivity in (17). So, we also compute results using a few alternative choices for these two parameters.

We first examine the effect of setting $r_s \equiv 0$, that is, neglecting the relatively small but appreciable stomatal resistance of well-watered transpiring leaves, as in many formulations of Penman–Monteith PET including those used by Burke et al. (2006) and Dai (2013), as well as in the case of pan evaporation. This gives an expression more in the spirit of Penman (1948) than Monteith (1981): the denominator of (5) simply becomes $\Delta + \gamma$. This choice should systematically increase f_Δ and thus reduce the percentage change in $\overline{\text{PET}}$ [by (17)], taking it even further from Clausius–Clapeyron. Indeed, the range of $\overline{\overline{f_\Delta}}$ shifts upward, to roughly 0.4–0.85 (not shown). However, the original range in Fig. 9 was about

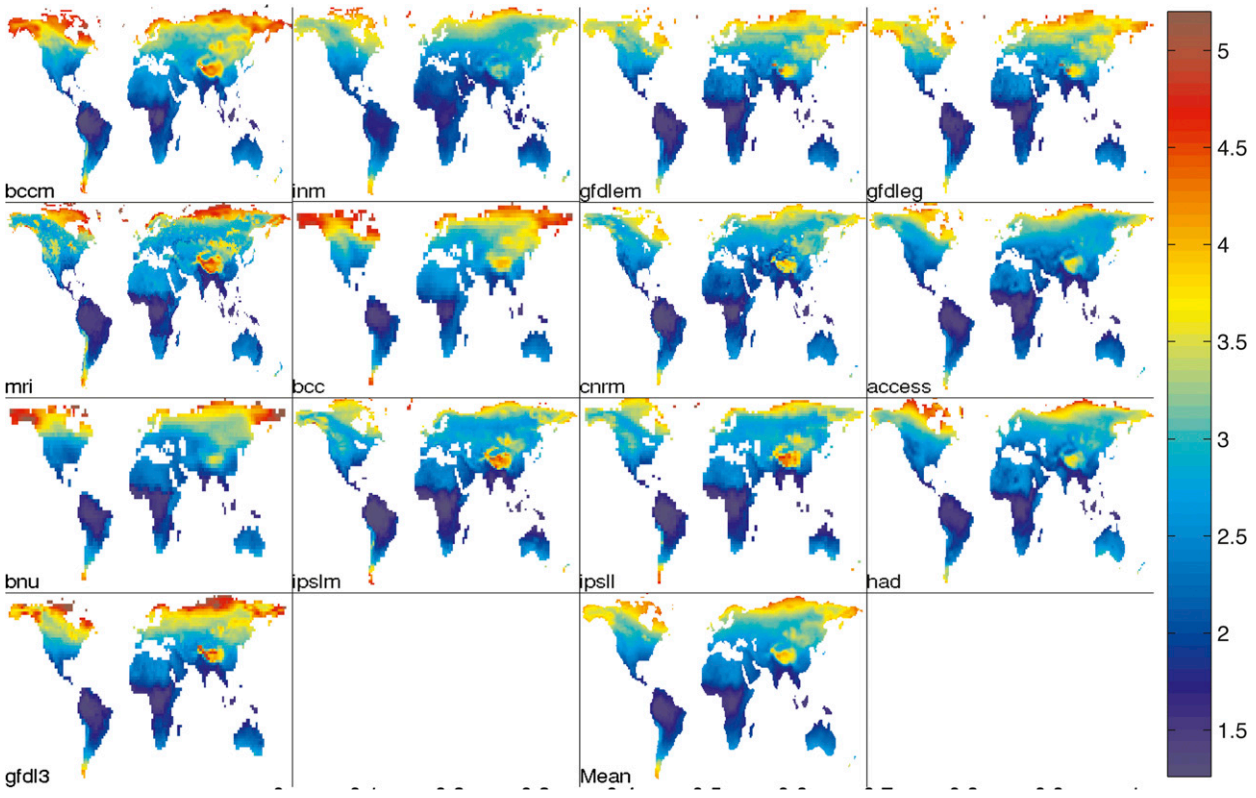

FIG. 11. Our scaling estimate $[d\Delta/(\Delta dT)(1-\overline{\overline{f_\Delta}})+\epsilon\overline{\overline{f_{\rm aero}}}]$ of the relative sensitivity of annual-mean PET to PET-weighted warming, from (17), in % °C^{-1}.

0.25–0.75, so this is a quantitative but not a qualitative increase. The spatial pattern of $\overline{\overline{f_\Delta}}$ hardly changes, except for losing some finescale structure owing to the loss of $|u|$ dependence.

Figure 14 shows the percentage changes in PET from changing T_a in this case. Comparison with the analogous Fig. 5 shows that setting $r_s \equiv 0$ indeed weakens the response, making single-digit- percentage values somewhat more common and values $> 30\%$ less common, but the patterns are very close. The at-a-point differences between the two figures are much less than the spatial and model-to-model variations within each figure, and the summary statistics in Table 2 differ by only about 2%–3% (of the basic state).

We also examine a ''smooth'' version of (5), in which the 0.5-m vegetation height h and thus the roughness lengths $z_{\rm om}$ and $z_{\rm oh}$ in (A1) are reduced by a factor of 10, setting h to a grasslike 5 cm and halving C_H from $\approx 5.7 \times 10^{-3}$ to $\approx 2.8 \times 10^{-3}$. [The Penman–Monteith formulations used in Burke et al. (2006), Dai (2013), and Feng and Fu (2013) also assume a smoother surface.] This, too, shifts the range of $\overline{\overline{f_\Delta}}$ only slightly upward, to roughly 0.35–0.8, with a very similar spatial pattern to the original in Fig. 9. So, the percentage change in $\overline{\rm PET}$ ends up looking almost identical to Fig. 5, but slightly (several percent) weaker (not shown). Again, the parameter-induced alterations in $d\overline{\rm PET}/\overline{\rm PET}$ are much less than the spatial and model-to-model variation.

Also, in the no-resistance case, adding this smooth vegetation would not appreciably lower the results any further because, in that case, C_H does not even appear in the denominator of (5) and thus can no longer affect $\overline{\overline{f_\Delta}}$. Thus, the effects are not additive—the no-resistance case gives a strict upper bound on $\overline{\overline{f_\Delta}}$ and an effective lower bound on warming-induced $d\overline{\rm PET}/\overline{\rm PET}$ (Fig. 14).

Finally, we examine a ''rough'', forestlike PET in which h, $z_{\rm om}$, and $z_{\rm oh}$ are *increased* by a factor of 10, setting h to 5 m and tripling C_H to $\approx 1.7 \times 10^{-2}$, a very large value. In this case, the range of $\overline{\overline{f_\Delta}}$ falls to roughly 0.15–0.7, again with a very similar spatial pattern to Fig. 9. Then $d\overline{\rm PET}/\overline{\rm PET}$ from T_a becomes somewhat larger than shown in Fig. 5, with values of 35%–40% or more becoming more widespread. Again, there is little qualitative or pattern change; the overall story is the same. In summary, widely different choices of vegetation parameters do not alter the big picture presented in sections 3 and 4 above.

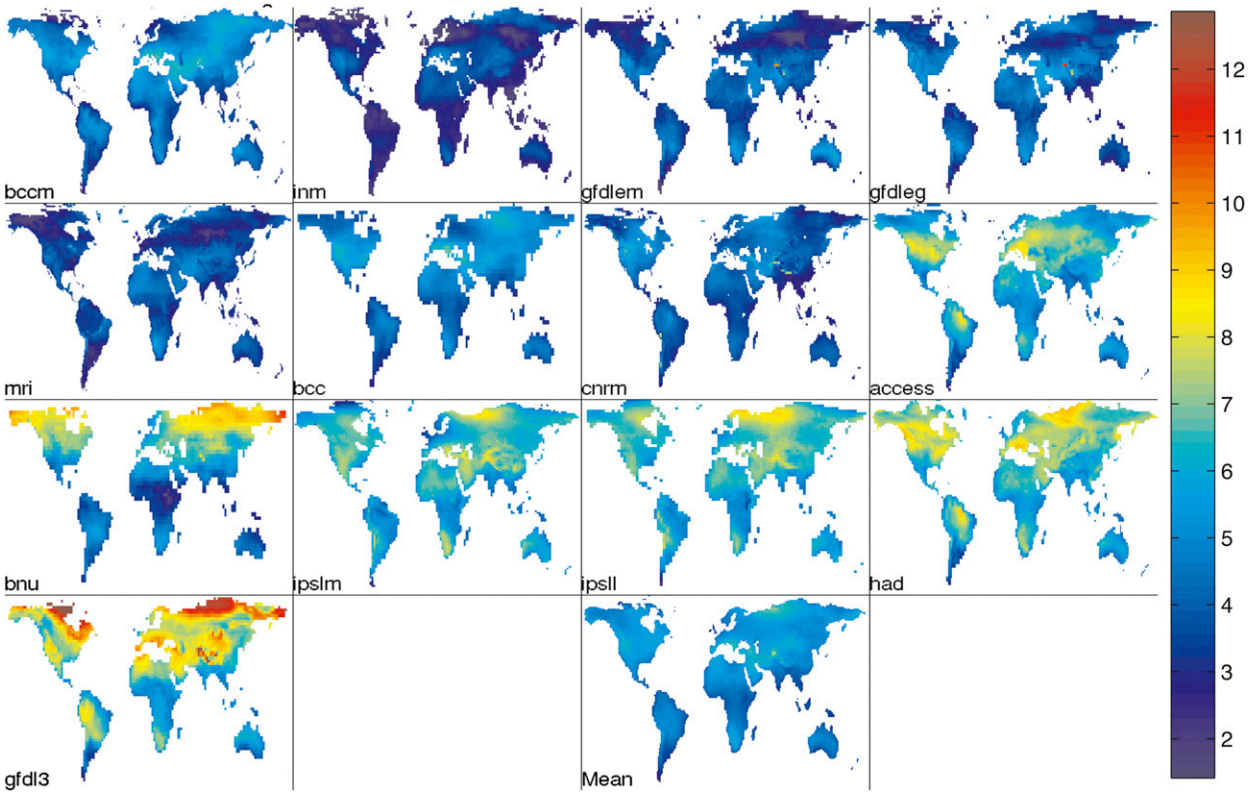

FIG. 12. PET-weighted annual average of climate warming $\overline{\overline{dT_a}}$ (°C) between 1981–99 and 2081–99.

There is also the question of whether r_s, like $(R_n - G)$, T_a, RH, and $|u|$ (and p_s), should have been treated as changing between the two epochs rather than staying fixed. After all, the carbon dioxide increase that causes greenhouse warming may also cause individual plant stomata to close (e.g., Sellers et al. 1996). However, there is still very large uncertainty about the bulk vegetation changes that will occur in concert with this, much larger than the uncertainty in the *climate* response to carbon dioxide (Huntingford et al. 2013). Almost nothing is known about this bulk response. Furthermore, the percentage sensitivity of Penman–Monteith PET (5) to a percentage change in r_s turns out to depend very strongly on the vegetation parameters r_s and C_H, in contrast to the much weaker dependence just presented in the case of sensitivity to T_a. Therefore, in this study we decided to only scale the PET response to climate change, and not the response to carbon-dioxide-induced plant physiological change.

6. Summary and discussion

Potential evapotranspiration (PET), the rate at which surface water evaporates if available in a given climate, has been projected to increase with future greenhouse warming in most or all locations, driving strong global trends toward drought (e.g., Dai 2013; Burke et al. 2006) and/or aridity (Feng and Fu 2013). In this study, we systematically analyzed the projected response of the Penman–Monteith equation (5), the fundamental physical quantification of PET used by those studies. We found that, at least in the 13 modern global climate models listed in Table 1, the main reason for the projected PET increase is the warming itself (Fig. 5), not the greenhouse-driven increase in surface net radiation (Fig. 4). The warming causes the PET increase by widening the vapor pressure deficit $e^*(1 - \mathrm{RH})$ corresponding to a given relative humidity RH, and/or by increasing the local slope $\Delta := de^*/dT$ of the Clausius–Clapeyron curve, which governs the partitioning between sensible and latent heat fluxes. Changes in RH are not of any strongly preferred sign and are not large enough to alter this.

The magnitude of the projected annual-mean PET increase between 1981–99 and a business-as-usual 2081–99 scenario is usually a low double-digit percentage (Figs. 5 and 3, Table 2), comparable to projections for local precipitation. This is because the numerator of Eq. (5) increases like Clausius–Clapeyron [5–6% $°C^{-1}$] with constant-RH warming, but in the denominator only the first term Δ increases similarly, while the second

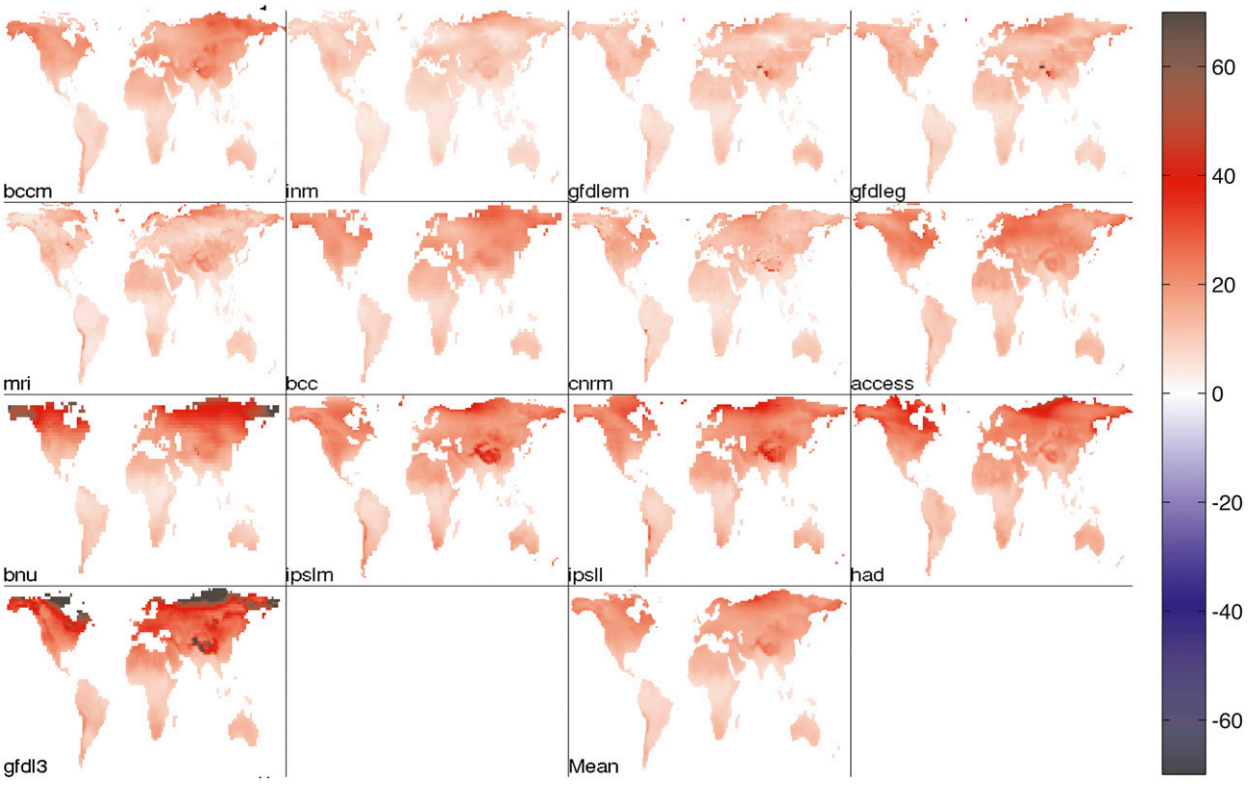

FIG. 13. Our scaling estimate [the exponential of (17) minus 1] for the percent changes in climatological annual-mean PET from setting only the ambient air temperature T_a to 2081–99 levels while leaving all other variables in (5), including RH, at 1981–99 levels (cf. Fig. 5). The last panel is the estimated percentage change in the multimodel mean given these estimates for each model.

term stays fixed. Thus, the net response of (5) to warming is sub-Clausius–Clapeyron, usually about 1.5–4% $°C^{-1}$ (Fig. 11). The higher values are found in cooler climates where Δ is smaller and thus less important in the denominator of (5) [i.e., $\overline{\overline{f_\Delta}}$ in (17) is smaller], and the lower values are found in warmer climates, explaining the strongly polar-amplified change pattern. Since the projected PET-weighted-mean warming for this scenario tends to be in the single digits of °C in most places (Fig. 12), the gross percentage response of PET to warming ends up in the lower double digits (Figs. 5 and 13). Large disagreement between models on the exact amount of warming produces similar disagreement on the total PET response. (The smaller but appreciable radiation- and RH-driven PET change components shown in Figs. 4 and 6 also vary widely between models, adding to the disagreement.)

A key, further advantage of our scaling approach (17) is that a climate model is not even needed for a user to locally compute the sensitivity of PET to future warming. All variables within the square brackets in (17) can be computed during routine calculations of observed present-day Penman–Monteith PET. For example, the values of $f_\Delta = \Delta/[\Delta + \gamma(1 + r_s C_H|u|)]$ and PET can be noted at each calculation time step and averaged over several years of data collection to obtain seasonally and/or diurnally resolved climatologies, which can then be used to find $\overline{\overline{f_\Delta}} = \overline{f_\Delta \cdot \mathrm{PET}}/\overline{\mathrm{PET}}$. If it turns out that $\overline{\overline{f_\Delta}}$ can be accurately estimated straight from $\Delta(\overline{T_a})$ and $\overline{\overline{|u|}}$, then the computation will be even simpler, as there will be no need to archive short-term values of f_Δ. So, whether the sensitivities plotted in Fig. 11 contain model biases is not actually that important for the practical use of (17).

We would also like to briefly give a more qualitative, physical explanation for why PET is less sensitive to T_a in warmer base climates. First, consider a climate cold enough that LH is unimportant in (3), even under well-watered conditions, and the dominant balance is between SH and $(R_n - G)$. In this climate, fixing $(R_n - G)$ effectively fixes SH, which fixes $(T_s - T_a)$ by (1). Now, if we rewrite (2) with the substitutions introduced later in section 1b,

$$\mathrm{LH} = \frac{\rho_a c_p[\Delta(T_s - T_a) + e^*(1 - \mathrm{RH})]}{\gamma(r_s + r_a)}, \qquad (18)$$

we can see that LH will be able to increase with temperature at a Clausius–Clapeyron rate, driven by Δ and e^*. Everything else in (18) is fixed by assumption.

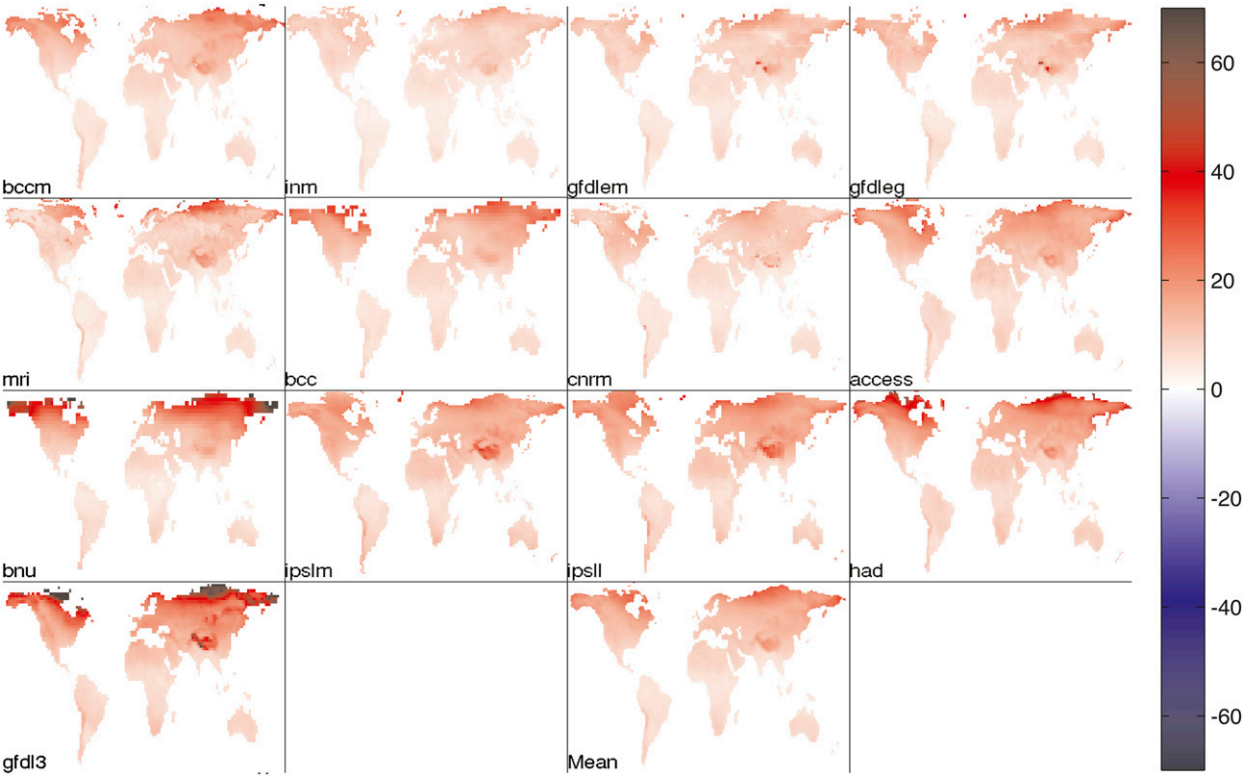

FIG. 14. Percent changes in climatological annual-mean PET from setting only the ambient air temperature T_a to 2081–99 levels while leaving all other variables in (5) at 1981–99 levels, for the version of (5) in which $r_s = 0$ (cf. Fig. 5).

However, as the climate warms and well-watered LH becomes appreciable, the evaporation will start to cool T_s relative to T_a and limit the fractional increase of (18). [Eventually, energy conservation (3) will start to severely limit the increase in well-watered LH, since $(R_n - G)$ is fixed here, and $(T_s - T_a)$ and SH can only go so negative owing to constraints involving the wet-bulb depression associated with our fixed RH.]

We also note that the PET percentage responses to changes in $(R_n - G)$, RH, and $|u|$, depicted in Figs. 4, 6, and 7, can also be analytically scaled in the manner demonstrated for T_a in section 4, with similar levels of success. However, the modeled changes in these variables (for input to these scalings) are not as well understood as the modeled warming dT_a, so these scalings do not provide as much understanding.

Finally, we are still interested in under what conditions or assumptions this large systematic PET increase with climate warming actually implies a systematic drying out of the land, as suggested by much of the work cited in section 1. To this end, we also have work in progress testing the sensitivity of modeled soil moisture to large changes in global temperature across a very wide range of continental geographies, forcing mechanisms, and land and atmospheric modeling choices.

Acknowledgments. The lead author would like to thank A. Dai for providing results on drought projections using different PET methods, and A. Swann for a key suggestion on section 4b. The authors also acknowledge the World Climate Research Programme's Working Group on Coupled Modelling, which is responsible for CMIP, and we thank the climate modeling groups (listed in Table 1) for producing and making available their model output. For CMIP the U.S. Department of Energy's Program for Climate Model Diagnosis and Intercomparison provides coordinating support and led development of software infrastructure in partnership with the Global Organization for Earth System Science Portals. This work was supported by NSF Grants AGS-0846641 and AGS-0936059.

APPENDIX

Detailed Methods

a. *Parameter and procedural choices for the Penman–Monteith equation*

Allen et al. (2005) provide parameters for two different reference vegetation types: short clipped grass,

and alfalfa (with the expectation that ''crop coefficients'' will be determined for conversion of the resulting potential evapotranspiration output to values suitable for other vegetation). We use the alfalfa values, reasoning that natural vegetation is closer to alfalfa in roughness and leafiness than it is to short clipped grass. Similarly, procedures are standardized separately for hourly and for daily calculation time steps; we use the hourly procedures on the 3-hourly model intervals. For meteorological variables, the model output is given as synoptic ''snapshots'' every 3 h, so for each interval we average the initial and final values of T_a, specific humidity q_a, and $|u|$ to estimate 3-h means, analogous to the hour means used by Allen et al. [Note that the raw output includes the wind components u and v but not the speed $|u|$, so $|u|$ has to be computed as $\sqrt{u^2 + v^2}$ at each snapshot before this averaging step. Also, two of the models (see Table 1) give u and v on a grid staggered by one-half the spacing in latitude and longitude from the main grid used for all the other variables, so we compute u at each main grid point as the mean of u at the four surrounding wind grid points, and similar for v, before this computation of $|u|$.]

With these choices of time step and vegetation type, the ASCE standardized procedures for variables in (5), and our few departures from them, are given as follows. A constant p_s is hydrostatically estimated from the surface elevation, but for simplicity we directly use the 3-hourly p_s output from the model, averaged like T_a and q_a above. The e^* is computed from the (3)-h-mean T_a using the empirical form $e^*(T) = 610.8 \exp[17.27T/(T + 237.3)]$, where e^* is in pascals and T is in degrees Celsius, and Δ using its derivative. Also, ρ_a is computed from the dry-air ideal gas law, using the (3)-h-mean T_a multiplied by 1.01 to account for virtual effects. A number of standardized methods are given to compute e_a from measurements; we directly use the 3-h-mean model q_a above, multiplying by p_s/ε to convert the units (nearly identical to their method 1). RH can then be computed as e_a/e^*. (In a few models this RH can occasionally slightly exceed 1, presumably due to interpolation; in these cases we set RH = 1 to avoid unphysical negative values of the aerodynamic term.) The L_v is idealized as a constant $2.45 \times 10^6\,\mathrm{J\,kg^{-1}}$. A field estimation method for R_n and a simple parameterization of G are given, but we simply compute $(R_n - G)$ from the model-output actual turbulent heat fluxes SH and LH using (3), which is still valid. These fluxes are already provided as 3-h means over our intervals, so there is no need for averaging. Then r_s is set at $30\,\mathrm{s\,m^{-1}}$ (''open'') during the day and $200\,\mathrm{s\,m^{-1}}$ (''closed'') at night, where ''day'' and ''night'' are defined as $R_n > 0$ and $R_n < 0$. We use $(R_n - G) > 0$ and $(R_n - G) < 0$ instead; this is justified since Allen et al. (2005) parameterize G as a small positive fraction of R_n.

For the transfer coefficient C_H, the standardized choice is the neutral, log-layer form,

$$C_H = \frac{k^2}{\ln[(z_w - d)/z_{\mathrm{om}}]\ln[(z_h - d)/z_{\mathrm{oh}}]}, \quad \text{(A1)}$$

where k is the von Kármán constant, z_w is the height of the wind speed measurements, z_{om} is the momentum roughness length, z_h is the height of the temperature and humidity measurements, z_{oh} is the scalar roughness length, and d is the zero-plane displacement. Allen et al. do not attempt to justify this choice, but one could argue that the great majority of PET is in warmer seasons or climates during the daytime, when the surface layer is either neutral or convective. For most wind speeds the Monin–Obukhov correction to C_H for convective conditions is much smaller than for stable conditions, so the worst of the potential problems are avoided. In any case, the standardized values for (A1) are as follows: k is set to 0.41, and z_w and z_h are each set to 2 m, although we use 10 m for z_w to match the height of the model wind output. If h is the assumed vegetation height (0.5 m for our standard alfalfa choice), z_{om} is set to $0.123h$, and z_{oh} to $0.0123h$. Finally, d is set to 0.08 m on the assumption that the weather measurements are taken over clipped grass, but we conservatively set $d = 0$ as it is not clear what exactly the model output heights are measured relative to. With these choices, C_H works out to $\approx 5.7 \times 10^{-3}$.

b. *Determining the PET responses to individual variables*

We would like to isolate the PET changes owing to changes in the individual inputs $(R_n - G)$, T_a, RH, and $|u|$. However, we cannot simply give (5) the 2081–99 time series for one of these and the 1981–99 time series for all other variables because the differing synoptic histories of the two epochs would destroy any interinput correlations other than the diurnal and annual cycles, adding an artificial change to the result. So, for each of these four inputs, we compute diurnally and annually varying climatologies for each model (as for PET), further smooth them with a 7-day running mean that respects the diurnal cycle, difference the two epochs (divide them, in the case of $|u|$), and perturb each year of the 1981–99 input time series by this diurnally and annually varying difference (factor), creating an input time series with the climatological properties of 2081–99 but the synoptic history of 1981–99. These can then be used one at a time in (5) to isolate the responses to $(R_n - G)$, T_a, RH, and $|u|$. [When we perturb $(R_n - G)$,

we still use the original 1981–99 ($R_n - G$) series to define day and night for setting r_s. Global warming may accomplish many feats, but it certainly will not transmute night into day! Consistent with this, when computing the 2081–99 PET in section 2, we subtract our diurnally and annually varying climatological difference from each year of the 2081–99 ($R_n - G$) series before it is used to define night and day.]

REFERENCES

Allen, R. G., I. A. Walter, R. Elliott, T. Howell, D. Itenfisu, and M. Jensen, 2005: The ASCE standardized reference evapotranspiration equation. American Society of Civil Engineers, 59 pp.

Arora, V. K., 2002: The use of the aridity index to assess climate change effect on annual runoff. *J. Hydrol.,* **265,** 164–177.

Brutsaert, W., and M. B. Parlange, 1998: Hydrologic cycle explains the evaporation paradox. *Nature,* **396,** 30.

Budyko, M. I., and D. H. Miller, 1974: *Climate and Life.* Academic Press, 508 pp.

Burke, E. J., S. J. Brown, and N. Christidis, 2006: Modeling the recent evolution of global drought and projections for the twenty-first century with the Hadley Centre climate model. *J. Hydrometeor.,* **7,** 1113–1125.

Dai, A., 2013: Increasing drought under global warming in observations and models. *Nat. Climate Change,* **3,** 52–58, doi:10.1038/NCLIMATE1633.

Feng, S., and Q. Fu, 2013: Expansion of global drylands under warming climate. *Atmos. Chem. Phys.,* **13,** 10 081–10 094.

Hartmann, D., 1994: *Global Physical Climatology.* Academic Press, 411 pp.

Held, I. M., and B. J. Soden, 2000: Water vapor feedback and global warming. *Annu. Rev. Energy Environ.,* **25,** 441–475, doi:10.1146/annurev.energy.25.1.441.

——, and ——, 2006: Robust responses of the hydrological cycle to global warming. *J. Climate,* **19,** 5686–5699.

Hobbins, M. T., A. Dai, M. L. Roderick, and G. D. Farquhar, 2008: Revisiting the parameterization of potential evaporation as a driver of long-term water balance trends. *Geophys. Res. Lett.,* **35,** L12403, doi:10.1029/2008GL033840.

Huntingford, C., and Coauthors, 2013: Simulated resilience of tropical rainforests to CO_2-induced climate change. *Nat. Geosci.,* **6,** 268–273, doi:10.1038/ngeo1741.

Lofgren, B. M., T. S. Hunter, and J. Wilbarger, 2011: Effects of using air temperature as a proxy for potential evapotranspiration in climate change scenarios of Great Lakes basin hydrology. *J. Great Lakes Res.,* **37,** 744–752, doi:10.1016/j.jglr.2011.09.006.

McKenney, M. S., and N. J. Rosenberg, 1993: Sensitivity of some potential evapotranspiration estimation methods to climate change. *Agric. For. Meteor.,* **64,** 81–110.

McVicar, T. R., T. G. Van Niel, L. T. Li, M. L. Roderick, D. P. Rayner, L. Ricciardulli, and R. J. Donohue, 2008: Wind speed climatology and trends for Australia, 1975–2006: Capturing the stilling phenomenon and comparison with near-surface reanalysis output. *Geophys. Res. Lett.,* **36,** L20403, doi:10.1029/2008GL035627.

——, and Coauthors, 2012: Global review and synthesis of trends in observed terrestrial near-surface wind speeds: Implications for evaporation. *J. Hydrol.,* **416-417,** 182–205, doi:10.1016/j.jhydrol.2011.10.024.

Meehl, G. A., and Coauthors, 2007: Global climate projections. *Climate Change 2007: The Physical Science Basis.* S. Solomon et al., Eds., Cambridge University Press, 747–845.

Middleton, N., and D. S. G. Thomas, 1997: *World Atlas of Desertification.* 2nd ed. Wiley, 182 pp.

Monteith, J. L., 1981: Evaporation and surface temperature. *Quart. J. Roy. Meteor. Soc.,* **107,** 1–27.

Mortimore, M., 2009: Dryland opportunities: A new paradigm for people, ecosystems and development. IUCN, IIED, and UNDP/DDC, 86 pp. [Available online at pubs.iied.org/pdfs/G02572.pdf.]

Palmer, W. C., 1965: Meteorological drought. U.S. Weather Bureau Research Paper 45, 58 pp.

Penman, H. L., 1948: Natural evaporation from open water, bare soil and grass. *Proc. Roy. Soc. London,* **193A,** 120–145, doi:10.1098/rspa.1948.0037.

Price, C., and D. Rind, 1994: The impact of a $2\times CO_2$ climate on lightning-caused fires. *J. Climate,* **7,** 1484–1494.

Pryor, S. C., and Coauthors, 2009: Wind speed trends over the contiguous United States. *J. Geophys. Res.,* **114,** D14105, doi:10.1029/2008JD011416.

Rind, D., R. Goldberg, J. Hansen, C. Rosenzweig, and R. Ruedy, 1990: Potential evapotranspiration and the likelihood of future drought. *J. Geophys. Res.,* **95** (D7), 9983–10 004.

Roderick, M. L., M. T. Hobbins, and G. D. Farquhar, 2009: Pan evaporation trends and the terrestrial water balance. II. Energy balance and interpretation. *Geogr. Compass,* **3** (2), 761–780, doi:10.1111/j.1749-8198.2008.00214.x.

Seager, R., and Coauthors, 2007: Model projections of an imminent transition to a more arid climate in southwestern North America. *Science,* **316,** 1181–1184, doi:10.1126/science.1139601.

Sellers, P., and Coauthors, 1996: Comparison of radiative and physiological effects of doubled atmospheric CO_2 on climate. *Science,* **271,** 1402–1406.

Taylor, K. E., R. J. Stouffer, and G. A. Meehl, 2012: An overview of CMIP5 and the experiment design. *Bull. Amer. Meteor. Soc.,* **93,** 485–498.

Thornthwaite, C. W., 1948: An approach toward a rational classification of climate. *Geogr. Rev.,* **38,** 55–94.

Wang, K., R. E. Dickinson, and S. Liang, 2012: Global atmospheric evaporative demand over land from 1973 to 2008. *J. Climate,* **25,** 8353–8361.

Wehner, M., D. R. Easterling, J. H. Lawrimore, R. R. Heim, R. S. Vose, and B. D. Santer, 2011: Projections of future drought in the continental United States and Mexico. *J. Hydrometeor.,* **12,** 1359–1377.